Materials and methods

Reagents. Synthesized α-GalCer was provided by Kirin Brewery Company (Gunma, Japan). LPS from *Escherichia coli* O55:B5 and Nω-nitro-L-arginine methyl ester hydrochloride (L-NAME) were purchased from Sigma Chemical Co. (St. Louis, MO, USA).

Mice. C57BL/6 mice at approximately 8 weeks of age were obtained from Japan SLC (Hamamatsu, Japan). IDO-knockout (KO) mice were obtained from Jackson Laboratory (Bar Harbor, ME, USA). All animal procedures were conducted in accordance with the National Institutes of Health Guide for the Care and Use of Laboratory Animals, and the guidelines for care and use of animals established by the Animal Care and Use Committee of Gifu University.

Cell preparation and culture. The mice were sacrificed at 0 h (non-treatment) and 12 h (α-GalCer-treatment) after intravenous administration of α-GalCer (1 μg/mouse). Peritoneal cells were obtained and suspended in RPMI 1640 medium (Wako Pure Chemical Industries, Osaka, Japan) containing 10% heat-inactivated fetal bovine serum (Thermo Fisher Scientific, Inc., Waltham, MA, USA) and cultured at 37 °C in a 5% CO_2 atmosphere.

Determination of nitrite concentration. Peritoneal cells from wild-type and IDO-KO mice were cultured with LPS (1–100 ng/mL) for 24 h. The nitrite concentration of the culture medium was estimated by the Griess reaction [19]. The culture medium (100 μL) was mixed with 100 μL of Griess reagent, and incubated at room temperature for 10 min, after which the absorbance was measured at 570 nm by using a microplate reader.

Assay of IDO activity. IDO activity was assessed using the methylene blue/ascorbate assay as described previously [20]. Briefly, the cell lysate was centrifuged at 7000*g* at 4 °C for 10 min. The supernatant (50 μL) was reacted with the substrate solution (50 μL) at 37 °C for 60 min. The substrate solution comprised 100 mM potassium phosphate buffer (pH 6.5), 50 μM methylene blue, 20 μg catalase, 50 mM ascorbate, and 0.4 mM L-tryptophan. After incubation, the samples were acidified with 3% perchloric acid and centrifuged at 7000*g* at 4 °C for 10 min. The concentration of L-kynurenine (L-KYN) was measured by high-performance liquid chromatography (HPLC). IDO activity was expressed as the L-KYN content per hour per milligram protein.

Real-time PCR analysis. Real-time reverse transcription polymerase chain reaction (RT-PCR) was used to quantify the levels of iNOS, IDO, IFN-γ, and TNF-α mRNA. Total RNA was isolated using an RNeasy mini kit (Qiagen GmbH, Hilden, Germany) and transcribed to cDNA by using the High capacity cDNA transcription kit (Applied Biosystems, Foster City, CA, USA). Purified cDNA was used as the template for real-time PCR conducted using pre-designed primer/probe sets for iNOS, IDO, IFN-γ, TNF-α, and 18S rRNA (Applied Biosystems), according to the manufacturer's recommendations. 18S rRNA was used as an internal control. Real-time PCR was carried out using a Light-Cycler Rapid Thermal Cycler System (Roche Diagnostic Systems, Indianapolis, IN, USA).

Western blot analysis. Peritoneal cells from α-GalCer-treated wild-type and IDO-KO mice were cultured with LPS (10 ng/mL) for 24 h. Protein (20 μg) from the cell lysate was subjected to sodium dodecyl sulfate–polyacrylamide gel electrophoresis (SDS–PAGE) and transferred to a nitrocellulose membrane. The membrane was blocked with 5% skim milk, and incubated with anti-NOS2, anti-IDO, and anti-GAPDH antibodies for 60 min at room temperature and subsequently incubated with peroxidase-labeled anti-mouse or anti-rabbit IgG for 60 min at room temperature. Immunoreactive protein bands were visualized with ECL plus (GE Healthcare UK Ltd., England).

Flow cytometric analysis. Flow cytometry was used to evaluate the phenotype of the peritoneal cells at 0 and 12 h after α-GalCer-treatment. Following reaction with anti-CD16/CD32 antibody to suppress non-specific binding, the peritoneal cells were stained with fluorescein-isothiocyanate (FITC)-conjugated anti-F4/80 antibody, phycoerythrin (PE)-conjugated anti-Toll-like receptor 4 (TLR4) antibody, FITC-conjugated anti-CD3 antibody, and PE-conjugated anti-DX5 antibody. The peritoneal cells were phenotypically characterized using FACScan (Becton–Dickinson, San Jose, CA, USA). CD3- and DX5-positive cells were considered as NKT cells, and F4/80- and TLR4-positive cells were considered as macrophages.

Statistical analysis. In each experiment, the results were expressed as means ± SD. The statistical significance of the difference in mean values was determined by Student's *t*-test or one-way analysis of variance followed by Scheffe's test. *P* values of less than 0.05 were considered significant.

Results

Effect of α-GalCer on LPS-induced NO production and IDO activity in peritoneal cells from wild-type and IDO-KO mice

To examine the effect of α-GalCer-pre-treatment on LPS-induced NO production, peritoneal cells (at a rate of 1×10^5 cells/well) from non-treated and α-GalCer-treated wild-type mice were cultured with 100 ng/mL LPS for 24 h. LPS-induced NO production was greater in peritoneal cells from α-GalCer-treated mice than in those from non-treated mice. In particular, the peritoneal cells obtained from the mice at 12 h after α-GalCer-treatment exhibited significantly greater LPS-induced NO production than those obtained after 6 and 48 h after α-GalCer-treatment (Fig. 1A), which was in keeping with the results of a previous report [8]. Therefore, peritoneal cells from the mice at 12 h after α-GalCer-treatment were used for the following experiments unless stated otherwise.

LPS-induced IDO activity was examined in peritoneal cells from wild-type and IDO-KO mice treated with or without α-GalCer. Peritoneal cells (at a rate of 3×10^6 cells/well) were cultured with 100 ng/mL LPS for 24 h. The LPS-induced IDO activity of the peritoneal cells from the α-GalCer-treated mice was markedly greater than that of cells from non-treated mice. On the other hand, IDO activity was not observed in the peritoneal cells from the IDO-KO mice (Fig. 1B).

Since previous reports suggested that NO interacts with IDO [17,18], we examined the effect of α-GalCer on LPS-induced NO production in wild-type and IDO-KO mice. Peritoneal cells from wild-type and IDO-KO mice treated with or without α-GalCer were cultured at a rate of 1×10^5 cells/well with LPS (1, 10, and 100 ng/mL) for 24 h. The extent of LPS-induced NO production was almost equal between the peritoneal cells from non-treated wild-type mice and IDO-KO mice (Fig. 1C). On the other hand, LPS-induced NO production was much greater in the peritoneal cells from α-GalCer-treated IDO-KO mice than in those from α-GalCer-treated wild-type mice (Fig. 1D).

LPS-induced mRNA and protein expression of iNOS and IDO in peritoneal cells from α-GalCer-treated wild-type and IDO-KO mice

As the second step in our experiment, we examined the expression of iNOS and IDO mRNA and protein in peritoneal cells from α-GalCer-treated wild-type and IDO-KO mice. The expression of iNOS and IDO mRNA in peritoneal cells stimulated with LPS (10 ng/mL) for 12 h was analyzed by real-time RT-PCR and was determined on the basis of 18S rRNA expression. No significant difference was observed in the expression of iNOS mRNA between the α-GalCer-treated wild-type and IDO-KO mice (Fig. 2A). The expression of IDO mRNA in the peritoneal cells from wild-type mice was significantly enhanced by LPS stimulation (Fig. 2B). The protein level

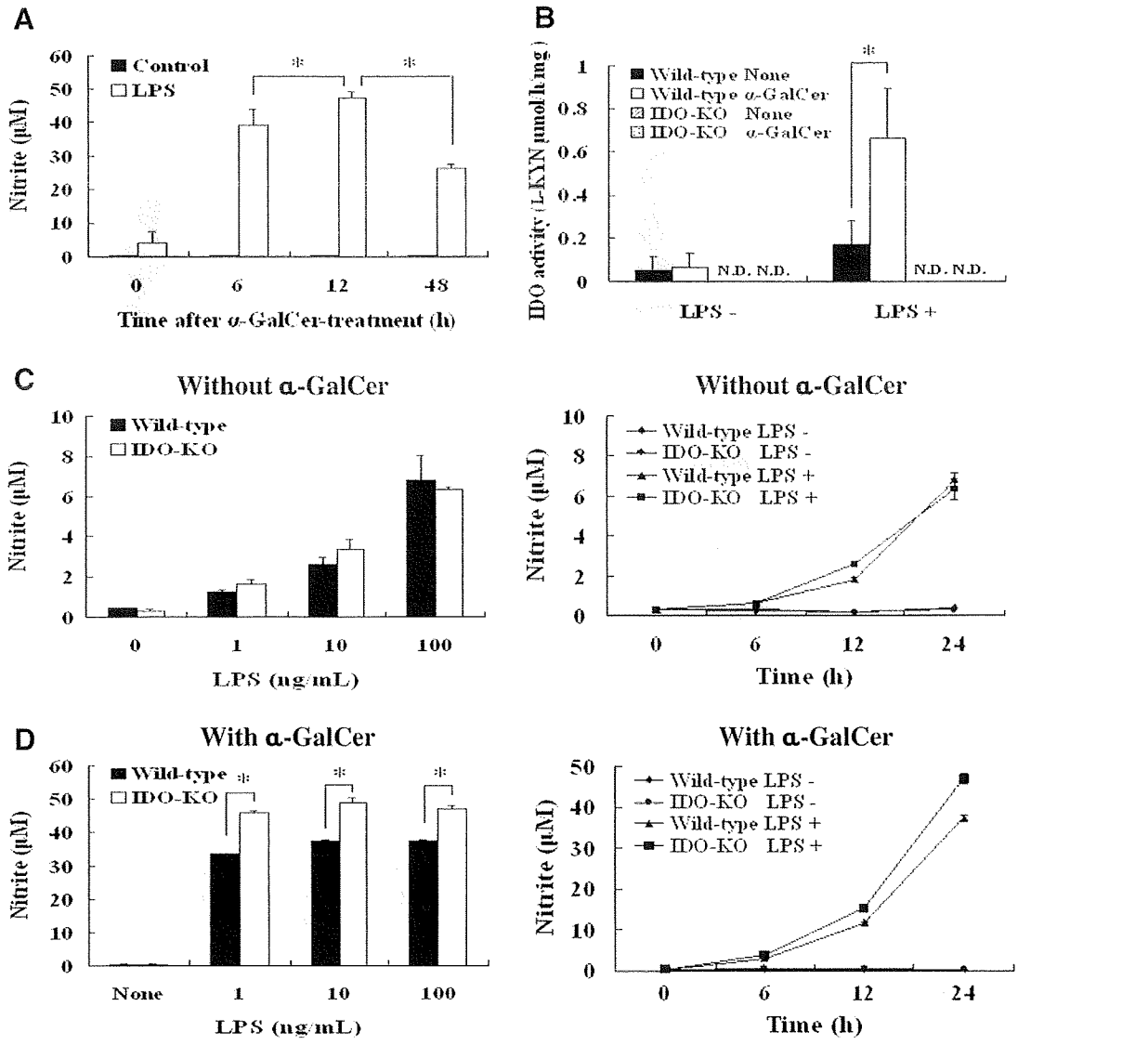

Fig. 1. Effect of α-GalCer on LPS-induced NO production and IDO activity in peritoneal cells. Peritoneal cells from the mice obtained at 0, 6, 12, and 48 h after α-GalCer-treatment were cultured at a rate of 1×10^5 cells/well with LPS (100 ng/mL), and the concentration of nitrite in the culture medium was determined (A). Peritoneal cells from non-treated and α-GalCer-treated wild-type and IDO-KO mice were cultured at a rate of 3×10^6 cells/well with LPS (100 ng/mL) for 24 h, and the IDO activity of the cell lysate was determined (B). Peritoneal cells from non-treated (C) and α-GalCer-treated (D) wild-type and IDO-KO mice were cultured at a rate of 1×10^5 cells/well with LPS (1, 10, and 100 ng/mL) for 24 h. In the time-course analysis of NO production, LPS was used at a concentration of 100 ng/mL. The data are represented as means ± SD of the results of three samples from each group. *$P < 0.05$; N.D.: not detected.

of iNOS and IDO in the peritoneal cells stimulated with LPS (10 ng/mL) for 24 h was examined by Western blot analysis and was determined on the basis of GAPDH protein expression. NO difference in the iNOS protein expression was observed between the α-GalCer-treated wild-type and IDO-KO mice. Further, in the wild-type mice, IDO protein was only expressed in the presence of LPS (Fig. 2C).

Effects of α-GalCer on IFN-γ and TNF-α expression and on the phenotype of peritoneal cells from wild-type and IDO-KO mice

Since Vα14 NKT cells activated by α-GalCer rapidly produce IFN-γ and TNF-α, which are closely related to iNOS expression, IFN-γ and TNF-α mRNA in peritoneal cells was analyzed at 0, 3, and 12 h after α-GalCer-treatment by using real-time PCR. There was no significant difference in the expression of IFN-γ and TNF-α mRNA between the wild-type and IDO-KO mice (Fig. 3A and B). Further, we examined the percentage of NKT cells (DX5- and CD3-positive cells) and macrophages (F4/80- and TLR4-positive cells) among the peritoneal cells from wild-type and IDO-KO mice by flow cytometry. No significant difference was observed in the ratio of CD3- and DX5-positive cells between the wild-type and IDO-KO mice treated and non-treated with α-GalCer (Fig. 3C). The ratio of F4/80- and TLR4-positive cells tended to be higher in the α-GalCer-treated mice than in the non-treated mice, but there was no significant difference between the wild-type and IDO-KO mice (Fig. 3D).

Effect of an NO inhibitor on LPS-induced IDO activity in peritoneal cells

Peritoneal cells from α-GalCer-treated wild-type mice (at a rate of 1×10^6 cells/well) were cultured with LPS (100 ng/mL) and L-NAME (4 mM) for 24 h. LPS-induced NO production by the peritoneal cells from α-GalCer-treated wild-type mice was significantly decreased by L-NAME, while the LPS-induced IDO activity was significantly increased by L-NAME (Fig. 4).

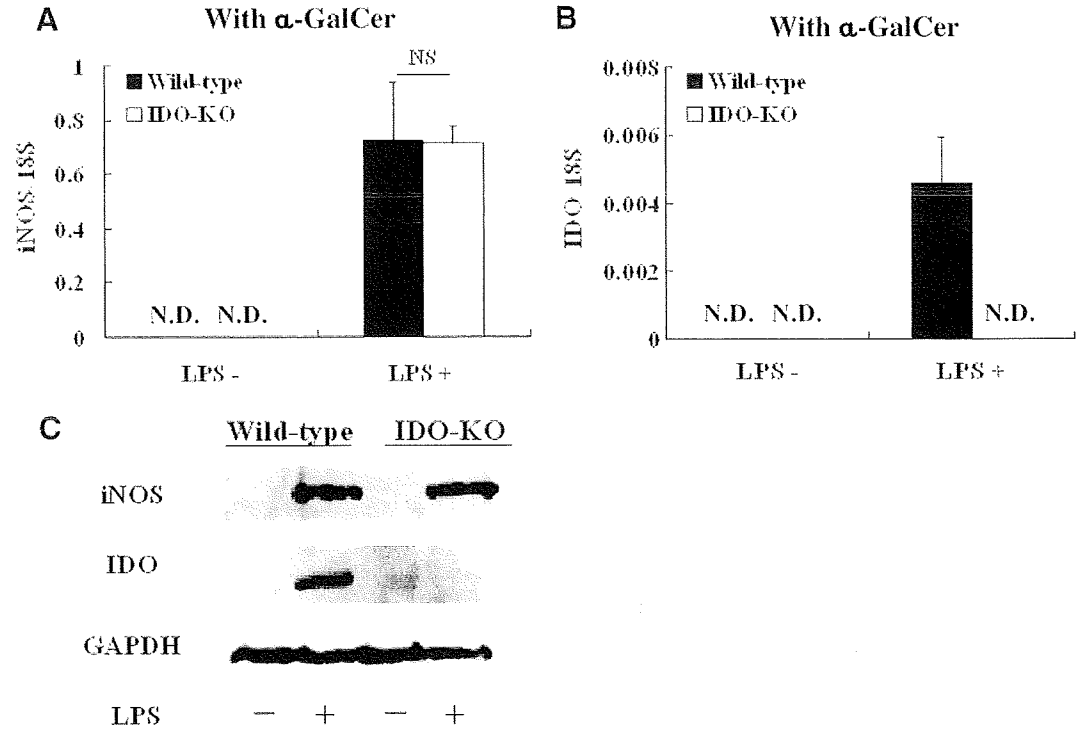

Fig. 2. LPS-induced mRNA and protein expression of iNOS and IDO in peritoneal cells from α-GalCer-treated wild-type and IDO-KO mice. The expression of iNOS and IDO mRNA in peritoneal cells from α-GalCer-treated mice stimulated with LPS (10 ng/mL) for 12 h was analyzed by real-time PCR and was determined on the basis of 18S rRNA expression (A, B). The data are represented as means ± SD of the results of three samples from each group. The expression of the iNOS and IDO proteins in peritoneal cells from α-GalCer-treated mice stimulated with LPS (10 ng/mL) for 24 h was examined by Western blot analysis and was based on the expression of the GAPDH protein (C). These experiments were repeated twice and produced the same results. $^{*}P < 0.05$; N.D.: not detected.

Discussion

In this study, we demonstrated that LPS-induced NO production and IDO activity were enhanced in mouse peritoneal cells obtained after α-GalCer-treatment (Fig. 1A and B). Interestingly, even in such conditions, these two molecules seemed to suppress each other (Figs. 1D and 4B). LPS-induced NO production reached its peak at 12 h after α-GalCer-treatment (Fig. 1A). Previous reports

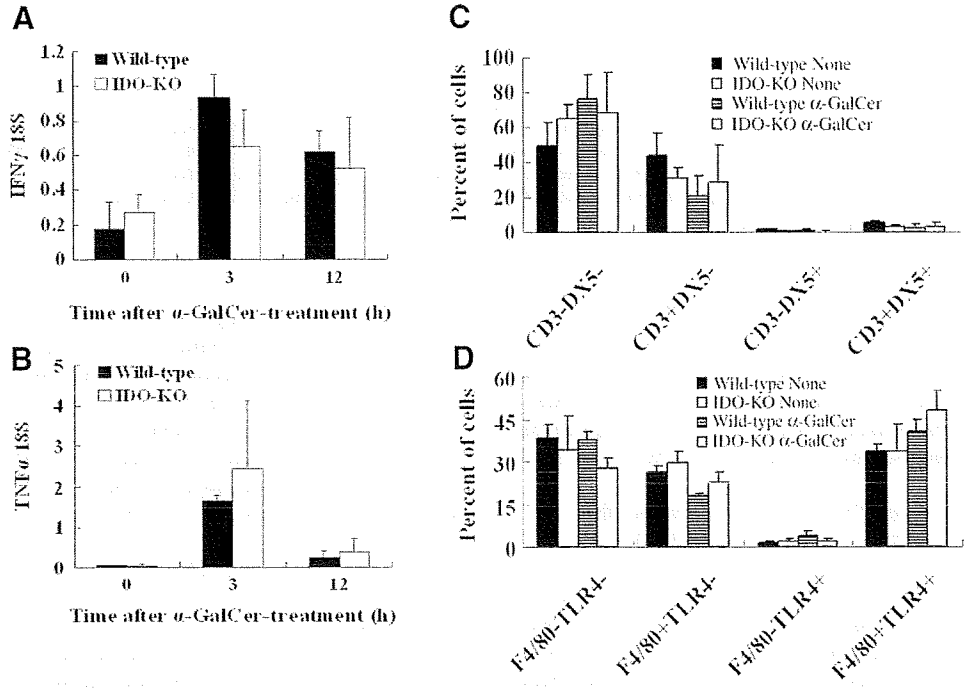

Fig. 3. Effects of α-GalCer on IFN-γ and TNF-α expression and on the phenotype of peritoneal cells from wild-type and IDO-KO mice. Expression of IFN-γ and TNF-α mRNA in peritoneal cells at 0, 3, and 12 h after α-GalCer-treatment was analyzed by real-time PCR and was determined on the basis of 18S rRNA expression (A, B). The percentage of NKT cells (DX5- and CD3-positive cells) and macrophages (F4/80- and TLR4-positive cells) among the peritoneal cells from the non-treated and α-GalCer-treated wild-type and IDO-KO mice was analyzed by flow cytometry (C, D). The data are represented means ± SD of the results of three mice from each group.

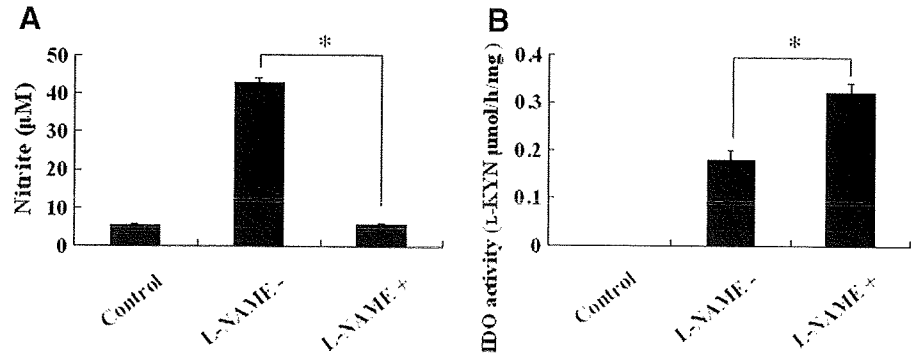

Fig. 4. Effect of an NO inhibitor on IDO activity in peritoneal cells. Peritoneal cells from α-GalCer-treated wild-type mice were cultured at a rate of 1×10^6 cells/well with LPS (100 ng/mL) and L-NAME (4 mM) for 24 h. Cells not treated with LPS were used as the control. The concentration of nitrite in the culture medium was determined (A), and the IDO activity of the cell lysate was determined (B). The data are represented as means ± SD of the results of three samples from each group. $^*P < 0.05$.

indicated that IFN-γ is a very important promoter of iNOS activity and that its production is high at 4–12 h after α-GalCer-treatment [9,21,22], so our results agree well with those of these previous studies. Furthermore, a minute amount of LPS may be adequate to cause inflammatory response in the presence of activated NKT cells, because LPS-induced NO production by peritoneal cells from α-GalCer-treated mice was almost the same at all LPS concentrations (Fig. 1D).

Previous reports suggested that NO interacts with IDO, and that IDO activity is inhibited by an NO donor or a peroxynitrite donor [17,18]. The nitration of the IDO protein inhibits IDO activity, and NO and peroxynitrite inhibit IDO activity in a concentration-dependent manner. It was shown that spermine NONOate and S-nitrosoglutathione markedly inhibit IDO activity at a concentration of over 25 μM. IDO activity was recovered by ceasing of the NO exposure, indicating that the inhibition of IDO activity was reversible. Since IDO mRNA and protein expression showed no changed in the presence of an NO donor, it can be inferred that NO post-translationally regulates IDO activity [18]. Our previous study demonstrated the presence of three nitrated peptides in the peroxynitrite-treated recombinant IDO digests and established the nitration of Tyrosine (Tyr)^{15}, Tyr^{345}, and Tyr^{353} residues by two-dimensional liquid chromatography/tandem mass spectrometry [17]. These studies consequently suggest that the nitration of tyrosine residues in the IDO protein by NO and peroxynitrite inhibits its IDO activity. In this study, we examined the difference in LPS-induced NO production by peritoneal cells between wild-type and IDO-KO mice. LPS-induced NO production was much higher in the peritoneal cells from α-GalCer-treated IDO-KO mice than in those from α-GalCer-treated wild-type mice (Fig. 1D). However, there was no significant difference in the expression of iNOS mRNA and protein between the wild-type and IDO-KO mice (Fig. 2). Moreover, there was no significant difference in the phenotype (CD3- and DX5-positive cell ratio or F4/80- and TLR4-positive cell ratio) of the peritoneal cells between the wild-type and IDO-KO mice treated or not treated with α-GalCer (Fig. 3C and D). These results show that iNOS was post-translationally regulated by the increased IDO activity. Since the IDO activity was enhanced by an NO inhibitor (Fig. 4), NO may be consumed during IDO inhibition, because of which its production is decreased in wild-type mice (Fig. 1D).

IDO is strongly induced by inflammatory cytokines particularly in macrophages and dendritic cells. Subsequent tryptophan deprivation inhibits T-cell proliferation and suppresses cell-mediated immunity [13,23]. Enhanced IDO activity also induces apoptosis of T cells and differentiation of naïve CD4-positive T cells into Treg cells [24], resulting in the attenuation of an extreme inflammatory response [25–27]. Thus, IDO is thought to play an important role in suppressing severe inflammation. It is suggested that inhibition of IDO activity by excess NO results in exacerbation of inflammation. A strong immune response in severe sepsis is thought to be critical in view of mortality, we previously reported that endotoxic shock is rapidly lethal in the presence of NKT cells activated by α-GalCer [28]. Because NKT cells are strongly activated by acute and chronic viral infections [29], secondary infection by bacteria under such conditions is expected to produce an extremely grave reaction. In the model of endotoxic shock sensitized by α-GalCer, it was confirmed that marked inflammation due to an extreme immune response is histologically observed in the lung and liver, and where iNOS is strongly expressed [9,30]. Our results suggest that a large amount of NO inhibits IDO, which has immunosuppressive function, resulting in further promotion of inflammation in severe endotoxic shock. It is therefore important to regulate IDO in such conditions.

In conclusion, we first reported the effect of Vα14 NKT cell activation on LPS-induced NO production and IDO activity by peritoneal cells from wild-type and IDO-KO mice. These findings may help elucidate the immune mechanism in intra-abdominal bacterial infection.

References

[1] M. Kronenberg, Toward an understanding of NKT cell biology: progress and paradoxes, Annu. Rev. Immunol. 23 (2005) 877–900.
[2] M. Taniguchi, M. Harada, S. Kojo, T. Nakayama, H. Wakao, The regulatory role of Valpha14 NKT cells in innate and acquired immune response, Annu. Rev. Immunol. 21 (2003) 483–513.
[3] R.B. Lorsbach, W.J. Murphy, C.J. Lowenstein, S.H. Snyder, S.W. Russell, Expression of the nitric oxide synthase gene in mouse macrophages activated for tumor cell killing. Molecular basis for the synergy between interferon-gamma and lipopolysaccharide, J. Biol. Chem. 268 (1993) 1908–1913.
[4] S. Ohya, Y. Tanabe, M. Makino, T. Nomura, H. Xiong, M. Arakawa, M. Mitsuyama, The contributions of reactive oxygen intermediates and reactive nitrogen intermediates to listericidal mechanisms differ in macrophages activated pre- and postinfection, Infect. Immun. 66 (1998) 4043–4049.
[5] G. Sass, K. Koerber, R. Bang, H. Guehring, G. Tiegs, Inducible nitric oxide synthase is critical for immune-mediated liver injury in mice, J. Clin. Invest. 107 (2001) 439–447.
[6] S.E. McKim, E. Gabele, F. Isayama, J.C. Lambert, L.M. Tucker, M.D. Wheeler, H.D. Connor, R.P. Mason, M.A. Doll, D.W. Hein, G.E. Arteel, Inducible nitric oxide synthase is required in alcohol-induced liver injury: studies with knockout mice, Gastroenterology 125 (2003) 1834–1844.
[7] H.M. Razavi, L. Wang, S. Weicker, G.J. Quinlan, S. Mumby, D.G. McCormack, S. Mehta, Pulmonary oxidant stress in murine sepsis is due to inflammatory cell nitric oxide, Crit. Care Med. 33 (2005) 1333–1339.
[8] P.L. Beck, Y. Li, J. Wong, C.W. Chen, C.M. Keenan, K.A. Sharkey, D.M. McCafferty, Inducible nitric oxide synthase from bone marrow-derived cells plays a critical role in regulating colonic inflammation, Gastroenterology 132 (2007) 1778–1790.
[9] H. Ohtaki, H. Ito, K. Ando, T. Ishikawa, K. Saito, M. Imawari, T. Yokochi, H. Moriwaki, M. Seishima, Valpha14 NKT cells activated by alpha-galactosylceramide augment lipopolysaccharide-induced nitric oxide production in mouse intra-hepatic lymphocytes, Biochem. Biophys. Res. Commun. 378 (2009) 579–583.

[10] H. Ito, N. Koide, A. Morikawa, F. Hassan, S. Islam, G. Tumurkhuu, I. Mori, T. Yoshida, S. Kakumu, H. Moriwaki, T. Yokochi, Augmentation of lipopolysaccharide-induced nitric oxide production by alpha-galactosylceramide in mouse peritoneal cells, J. Endotoxin Res. 11 (2005) 213–219.
[11] T.W. Stone, L.G. Darlington, Endogenous kynurenines as targets for drug discovery and development, Nat. Rev. Drug Discov. 1 (2002) 609–620.
[12] U. Grohmann, F. Fallarino, P. Puccetti, Tolerance, DCs and tryptophan: much ado about IDO, Trends Immunol. 24 (2003) 242–248.
[13] A.L. Mellor, D.H. Munn, IDO expression by dendritic cells: tolerance and tryptophan catabolism, Nat. Rev. Immunol. 4 (2004) 762–774.
[14] F. Fallarino, U. Grohmann, K.W. Hwang, C. Orabona, C. Vacca, R. Bianchi, M.L. Belladonna, M.C. Fioretti, M.L. Alegre, P. Puccetti, Modulation of tryptophan catabolism by regulatory T cells, Nat. Immunol. 4 (2003) 1206–1212.
[15] U. Grohmann, C. Volpi, F. Fallarino, S. Bozza, R. Bianchi, C. Vacca, C. Orabona, M.L. Belladonna, E. Ayroldi, G. Nocentini, L. Boon, F. Bistoni, M.C. Fioretti, L. Romani, C. Riccardi, P. Puccetti, Reverse signaling through GITR ligand enables dexamethasone to activate IDO in allergy, Nat. Med. 13 (2007) 579–586.
[16] D.H. Munn, M.D. Sharma, J.R. Lee, K.G. Jhaver, T.S. Johnson, D.B. Keskin, B. Marshall, P. Chandler, S.J. Antonia, R. Burgess, C.L. Slingluff Jr., A.L. Mellor, Potential regulatory function of human dendritic cells expressing indoleamine 2,3-dioxygenase, Science 297 (2002) 1867–1870.
[17] H. Fujigaki, K. Saito, F. Lin, S. Fujigaki, K. Takahashi, B.M. Martin, C.Y. Chen, J. Masuda, J. Kowalak, O. Takikawa, M. Seishima, S.P. Markey, Nitration and inactivation of IDO by peroxynitrite, J. Immunol. 176 (2006) 372–379.
[18] S.R. Thomas, A.C. Terentis, H. Cai, O. Takikawa, A. Levina, P.A. Lay, M. Freewan, R. Stocker, Post-translational regulation of human indoleamine 2,3-dioxygenase activity by nitric oxide, J. Biol. Chem. 282 (2007) 23778–23787.
[19] L.C. Green, D.A. Wagner, J. Glogowski, P.L. Skipper, J.S. Wishnok, S.R. Tannenbaum, Analysis of nitrate, nitrite, and [15N]nitrate in biological fluids, Anal. Biochem. 126 (1982) 131–138.
[20] S. Fujigaki, K. Saito, K. Sekikawa, S. Tone, O. Takikawa, H. Fujii, H. Wada, A. Noma, M. Seishima, Lipopolysaccharide induction of indoleamine 2,3-dioxygenase is mediated dominantly by an IFN-gamma-independent mechanism, Eur. J. Immunol. 31 (2001) 2313–2318.
[21] H. Kitamura, K. Iwakabe, T. Yahata, S. Nishimura, A. Ohta, Y. Ohmi, M. Sato, K. Takeda, K. Okumura, L. Van Kaer, T. Kawano, M. Taniguchi, T. Nishimura, The natural killer T (NKT) cell ligand alpha-galactosylceramide demonstrates its immunopotentiating effect by inducing interleukin (IL)-12 production by dendritic cells and IL-12 receptor expression on NKT cells, J. Exp. Med. 189 (1999) 1121–1128.
[22] H. Kitamura, A. Ohta, M. Sekimoto, M. Sato, K. Iwakabe, M. Nakui, T. Yahata, H. Meng, T. Koda, S. Nishimura, T. Kawano, M. Taniguchi, T. Nishimura, Alpha-galactosylceramide induces early B-cell activation through IL-4 production by NKT cells, Cell. Immunol. 199 (2000) 37–42.
[23] D.H. Munn, M. Zhou, J.T. Attwood, I. Bondarev, S.J. Conway, B. Marshall, C. Brown, A.L. Mellor, Prevention of allogeneic fetal rejection by tryptophan catabolism, Science 281 (1998) 1191–1193.
[24] F. Fallarino, U. Grohmann, C. Vacca, R. Bianchi, C. Orabona, A. Spreca, M.C. Fioretti, P. Puccetti, T cell apoptosis by tryptophan catabolism, Cell Death Differ. 9 (2002) 1069–1077.
[25] L. Romani, F. Fallarino, A. De Luca, C. Montagnoli, C. D'Angelo, T. Zelante, C. Vacca, F. Bistoni, M.C. Fioretti, U. Grohmann, B.H. Segal, P. Puccetti, Defective tryptophan catabolism underlies inflammation in mouse chronic granulomatous disease, Nature 451 (2008) 211–215.
[26] L. Romani, T. Zelante, A. De Luca, F. Fallarino, P. Puccetti, IL-17 and therapeutic kynurenines in pathogenic inflammation to fungi, J. Immunol. 180 (2008) 5157–5162.
[27] L. Romani, P. Puccetti, Protective tolerance to fungi: the role of IL-10 and tryptophan catabolism, Trends Microbiol. 14 (2006) 183–189.
[28] H. Ito, N. Koide, F. Hassan, S. Islam, G. Tumurkhuu, I. Mori, T. Yoshida, S. Kakumu, H. Moriwaki, T. Yokochi, Lethal endotoxic shock using alpha-galactosylceramide sensitization as a new experimental model of septic shock, Lab. Invest. 86 (2006) 254–261.
[29] C.A. Biron, L. Brossay, NK cells and NKT cells in innate defense against viral infections, Curr. Opin. Immunol. 13 (2001) 458–464.
[30] G. Tumurkhuu, N. Koide, J. Dagvadorj, A. Morikawa, F. Hassan, S. Islam, Y. Naiki, I. Mori, T. Yoshida, T. Yokochi, The mechanism of development of acute lung injury in lethal endotoxic shock using alpha-galactosylceramide sensitization, Clin. Exp. Immunol. 152 (2008) 182–191.

Biochemical and Biophysical Research Communications 378 (2009) 579–583

Contents lists available at ScienceDirect

Biochemical and Biophysical Research Communications

journal homepage: www.elsevier.com/locate/ybbrc

Vα14 NKT cells activated by alpha-galactosylceramide augment lipopolysaccharide-induced nitric oxide production in mouse intra-hepatic lymphocytes

Hirofumi Ohtaki [a], Hiroyasu Ito [a,*], Kazuki Ando [a], Tetsuya Ishikawa [c], Kuniaki Saito [d], Michio Imawari [e], Takashi Yokochi [f], Hisataka Moriwaki [b], Mitsuru Seishima [a]

[a] Department of Informative Clinical Medicine, Gifu University Graduate School of Medicine, 1-1 Yanagido, Gifu 501-1194, Japan
[b] First Department of Internal Medicine, Gifu University Graduate School of Medicine, 1-1 Yanagido, Gifu 501-1194, Japan
[c] Cancer Immunotherapy Center, Nagoya Kyoritsu Hospital, 1-195 Hoge, Nakagawa, Nagoya, Aichi 454-0933, Japan
[d] Human Health Sciences, Graduate School of Medicine and Faculty of Medicine, Kyoto University, 53 Kawahara-cho, Shogoin, Sakyo, Kyoto 606-8507, Japan
[e] Second Department of Internal Medicine, Showa University School of Medicine, 1-5-8 Hatanodai, Shinagawa-ku, Tokyo 142-8666, Japan
[f] Department of Microbiology and Immunology, Aichi Medical University, Nagakute, Aichi 480-1195, Japan

ARTICLE INFO

Article history:
Received 10 November 2008
Available online 3 December 2008

Keywords:
Vα14 NKT cell
α-Galactosylceramide
Lipopolysaccharide
Nitric oxide
Intra-hepatic lymphocytes

ABSTRACT

Vα14 natural killer T (Vα14 NKT) cells activated by α-galactosylceramide (α-GalCer) secrete a large amount of Th1 and Th2 cytokines. IFN-γ plays a crucial role in the inflammation response, and is also known as an activator of nitric oxide (NO) production. We previously reported that lipopolysaccharide (LPS)-induced NO production is augmented by α-GalCer in mouse peritoneal cells. Since the liver is susceptible to LPS stimulation via the portal vein, we examined the effect of α-GalCer on LPS-induced NO production in murine intra-hepatic lymphocytes (IHLs). Although IHLs augmented LPS-induced NO production by α-GalCer administration, such an augmentation was not observed in non-treated mice. Furthermore, α-GalCer did not augment LPS-induced NO production in IHLs from IFN-γ knockout mice. In flow cytometry analysis of IHLs from α-GalCer-treated mice, the ratio and number of F4/80- and TLR4-positive cells rose as compared with non-treated mice. The liver injury may be induced by LPS and NO under the condition where Vα14 NKT cells were activated.

α-Galactosylceramide (α-GalCer), a glycolipid antigen, specifically activates Vα14 natural killer T (NKT) cells via a CD1d-restricted mechanism. Vα14 NKT cells are a lymphoid lineage characterized by expression of invariant T-cell receptor (TCR) encoded by Vα14-Jα18 gene segments. These cells play a regulatory role in the immunological response under various pathological conditions, including tumor formation, autoimmune diseases, allergy, and infection, by rapidly secreting a large amount of Th1 and Th2 cytokines [1–3]. Additionally, IFN-γ, representative of Th1 cytokines, has been known to elevate nitric oxide (NO) production [4,5].

NO exhibits a wide range of important functions *in vivo*, acting as a relaxing factor mediating vasodilatation, a neuronal messenger molecule, a major regulatory molecule and a principal cytotoxic mediator of the immune system [6–8]. The signal (messenger) molecule NO is synthesized by constitutively expressed NO synthase (cNOS) for short periods of time. The killer (cytotoxic) molecule NO is synthesized by an inducible isoform of NOS (iNOS) that, once expressed, produces NO for long periods of time. It appears paradoxical that NO can both act as a physiological intercellular messenger and display cytotoxic activity *in vivo* [8]. Already, a number of studies have examined the relationship between NO production and tissue injury [9–13]. It was previously reported that NO plays an important role in alcohol-induced liver injury [14], hemorrhagic shock [15], concanavalin A-induced liver injury [16–18], liver damage after GalN/LPS treatment [10], and mycobacterial liver injury [19].

Our previous study reported augmentation of LPS-induced NO production by α-GalCer in mouse peritoneal cells through the release of IFN-γ from Vα14 NKT cells [20]. We thus focused on the liver, which is easily subjected to LPS stimulation via the portal vein and recruits many NKT cells. If α-GalCer augments LPS-induced NO production in intra-hepatic lymphocytes (IHLs), it may give us a clue to understand the association between NO and liver injury under conditions of activated NKT cells. Therefore, the aim of our study was to investigate the effect of α-GalCer on LPS-induced NO production in murine IHLs.

* Corresponding author. Fax: +81 58 230 6431.
E-mail address: hito@gifu-u.ac.jp (H. Ito).

0006-291X/$ - see front matter © 2008 Elsevier Inc. All rights reserved.
doi:10.1016/j.bbrc.2008.11.075

Materials and methods

Reagents. Synthesized α-GalCer was provided by Kirin Brewery Company (Gunma, Japan). LPS from *Escherichia coli* O55:B5 was purchased from Sigma Chemical Co. (St. Louis, MO, USA).

Mice. C57BL/6 and BALB/c mice at approximately 10 weeks of age were obtained from Japan SLC (Hamamatsu, Japan). IFN-γ knockout (−/−) mice were obtained from Jackson Laboratory (Bar Harbor, ME, USA). Jα18 −/− mice as Vα14 NKT cell-deficient mice were kindly provided by T. Nakayama, Chiba University and M. Taniguchi, RIKEN Research Centre. All procedures were conducted in accordance with the National Institutes of Health Guide for the Care and Use of Laboratory Animals, and with the guidelines for care and use of animals established by the Animal Care and Use Committee of Gifu University.

Cell preparation and culture. The mice were sacrificed after intravenous administration of α-GalCer (1 μg/mouse). Liver was perfused with heparinized sterile saline to remove peripheral blood cells, and liver homogenate was passed through stainless steel mesh. IHLs were obtained by the centrifugation of liver homogenate with Ficoll–Hypaque. IHLs were suspended in RPMI 1640 medium containing 10% heat-inactivated fetal calf serum (GIBCO-BRL, Gaithersburg, MD, USA) and 1×10^5 cells/200 μL were seeded on a 96-well microplate, after which LPS was added. After 24 h at 37 °C under 5% CO_2, culture supernatants and IHLs were collected for NO and iNOS mRNA determinations.

Nitrite determination. The nitrite accumulated in the culture medium was measured as an indicator of NO production based on the Griess reaction [21]. The culture supernatant (100 μL) was mixed with 100 μL of Griess reagent, incubated at room temperature for 10 min, and then the absorbance was measured at 570 nm using a microplate reader.

Real-time PCR. Real-time PCR (RT-PCR) was used to quantify the level of iNOS mRNA. Measurements of iNOS mRNA were made in IHL-stimulated by LPS for 24 h with or without α-GalCer. Total RNA was isolated using an Rneasy mini kit (Qiagen GmbH, Hilden, Germany) and modified to cDNA using the Omniscript reverse transcriptase kit (Qiagen). The purified cDNA was used as a template for RT-PCR using predesigned primer/probe sets for the iNOS gene (Assays On Demand; Applied Biosystems, Foster City, CA, USA) and 2× Taqman Universal PCR Master Mix (Applied Biosystems) according to the manufacturer's recommendations. Predesigned primer/probe sets for 18 S were used as an internal control in each reaction well (Applied Biosystems). RT-PCR was carried out using a Light Cycler Rapid Thermal Cycler System (Roche Diagnostic Systems, Indianapolis, USA).

Flow cytometry analysis. Flow cytometry was used to evaluate TLR4 and F4/80 expression of IHLs with or without α-GalCer administration. IHLs were obtained from mice 0, 6 and 12 h after α-GalCer-administration. Following reaction with anti-CD16/CD32 antibody to suppress nonspecific binding, IHLs were stained with fluorescein-isothiocyanate (FITC)-conjugated anti-F4/80 antibody and phycoerythrin (PE)-conjugated anti-TLR4 antibody. The phenotypic characterization of IHLs was carried out using FACScan (Becton-Dickinson, San Jose, CA, USA).

Isolation of CD11b*-positive cells.* IHLs from mice were separated into CD11b-positive and negative cells using anti-CD11b-conjugated magnetic beads (Miltenyi Biotec GmbH, Bergisch Gladbach, Germany). The magnetically labeled cells were purified using VarioMACS system (Miltenyi Biotec GmbH).

Statistical analysis. In each experiment, the results were expressed as mean ± SD. Statistical significance of the difference in mean values was determined by Student's *t*-test, and *p* values of less than 0.05 were considered to be significant.

Results

Effect of α-GalCer on LPS-induced NO production in IHLs

IHLs from non-treated and α-GalCer-treated wild-type mice were cultured at $1x10^5$ cells/well with LPS for 24 h. The concentration of nitrite was determined in culture supernatant. IHLs from the mice at 6 h after α-GalCer treatment produced a little amount of NO in the presence of LPS (0.1 μg/mL), and IHLs from the mice at 12 h after treatment produced a large amount of LPS-induced NO. On the other hand, IHLs from the mice at 0 and 48 h after treatment scarcely produced LPS-induced NO (Fig. 1A). Therefore, IHLs from the mice at 12 h after α-GalCer-treatment were used for the following experiments unless otherwise stated. IHLs from non-treated mice did not produce NO in the presence of high concentrations of LPS (1 and 10 μg/mL) (Fig. 1B). On the other hand, NO production was significantly augmented in IHLs from mice treated with α-GalCer in the presence of low concentrations of LPS (Fig. 1C).

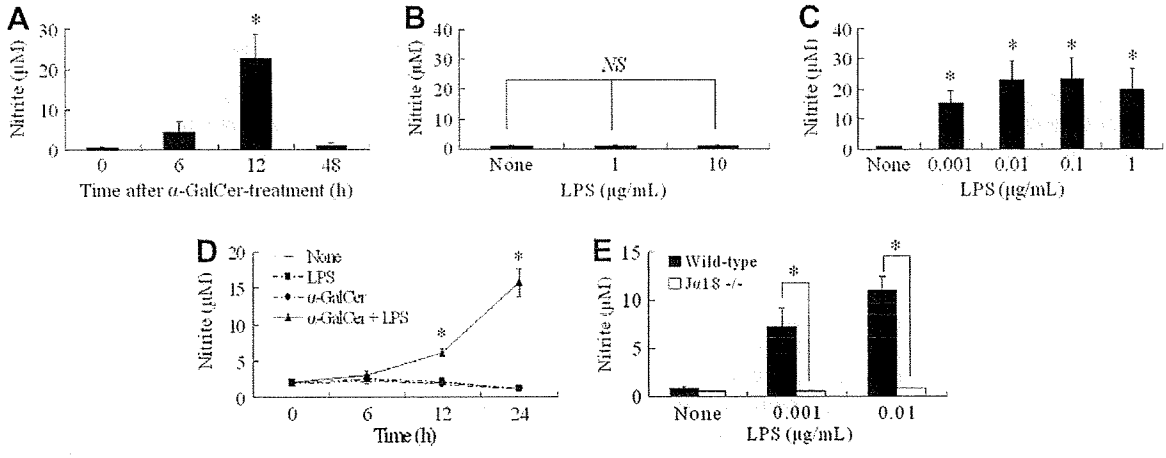

Fig. 1. Effect of α-GalCer on LPS-induced NO production in IHLs. IHLs from the mice at 0, 6, 12 and 48 h after α-GalCer-treatment were cultured at 1×10^5 cells/well with LPS (0.1 μg/mL) (A). In experiment of LPS concentration dependence, IHLs were cultured at 1×10^5 cells/well with LPS. LPS concentration used was 1, 10 μg/mL in non-treated-IHLs (B), and 0.001, 0.01, 0.1, 1 μg/mL in α-GalCer-treated-IHLs (C). The concentration of nitrite in the supernatant was determined 24 h after LPS stimulation. In time course of NO production, LPS concentration used was 10 μg/mL in non-treated-IHLs, and 0.1 μg/mL in α-GalCer-treated-IHLs. The concentration of nitrite in the supernatant was determined 6, 12, and 24 h after LPS stimulation (D). IHLs from α-GalCer-treated wild-type and Jα-281 −/− mice were cultured at 1×10^5 cells/well with LPS (0.001 and 0.01 μg/mL). The concentration of nitrite in the supernatant was determined 24 h after LPS stimulation (E). The data represented are means ± SD from 3 mice of each group. *NS*, not significant; $^*p < 0.05$ vs. 0 h or none.

In time course of LPS-induced NO production, IHLs (1×10^5 cells/well) from non-treated and α-GalCer-treated wild-type mice were stimulated with LPS (non-treated mice:10 μg/ml, α-GalCer-treated mice:0.1 μg/ml) for 6, 12, and 24 h. LPS-induced NO production in IHLs from α-GalCer-treated mice increased after 12 h and at 24 h reached approximately twice that at 12 h. On the other hand, the enhancement of NO production was not observed in IHLs from non-treated mice through 24 h (Fig. 1D).

To examine direct effect by α-GalCer, IHLs from α-GalCer-treated wild-type and Jα18 −/− mice were cultured at 1×10^5 cells/well with LPS (0.001 and 0.01 μg/mL) for 24 h. Although IHLs from wild-type mice augmented LPS-induced NO production, such an augmentation was not observed in Jα18 −/− mice (Fig. 1E).

Comparison of NO production and iNOS mRNA level between wild-type and IFN-γ −/− mice with α-GalCer administration

IHLs from the wild-type and IFN-γ −/− mice at 12 h after α-GalCer-treatment were cultured at 1×10^5 cells/well with LPS for 24 h. Culture supernatant was used for the determination of nitrite. NO production in IHLs from α-GalCer-treated wild- type mice significantly increased with LPS stimulation. On the other hand, α-GalCer did not augment LPS-induced NO production in IHLs from IFN-γ −/− mice (Fig. 2A).

The expression of iNOS mRNA in IHLs stimulated with LPS was examined with real-time RT-PCR and was determined based on 18S mRNA. IHLs from wild-type mice and IFN-γ −/− mice with or without α-GalCer administration were cultured at 1×10^5 cells/well with LPS for 24 h. The expression of iNOS mRNA in IHLs from α-GalCer-treated wild-type mice was significantly enhanced with LPS stimulation, but that in IHLs from α-GalCer-treated IFN-γ −/− mice was not (Fig. 2B).

Identification of NO producing cells

CD11b-positive and CD11b-negative cells in IHLs from the wild-type mice at 0 and 12 h after α-GalCer-treatment were isolated by magnetic cell sorting. Each cell type was cultured at 1×10^5 cells/200 μL with LPS (1 μg/mL) for 24 h. Culture supernatant was subjected for determination of the nitrite concentration. LPS-induced NO production was significantly augmented in CD11b-positive cells from α-GalCer-treated mice. On the other hand, in CD11b-negative cells from α-GalCer-treated mice and each cells from non-treated mice, such an enhancement of LPS-induced NO production was not observed (Fig. 3).

Effect of α-GalCer on cell ratio and cell number of F4/80 and TLR4 double-positive cell in IHLs

Next, by reason that CD11b-positive cells significantly produced LPS-induced NO, we examined the ratio and number of F4/80- and

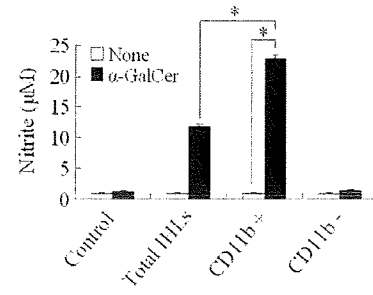

Fig. 3. Identification of NO producing cells. CD11b-positive cells were isolated from IHLs of non- and α-GalCer-treated wild-type mice by magnetic cell sorting. Each cells (total IHLs, CD11b-positive IHLs and CD11b-negative IHLs) was cultured at 1×10^5 cells/200 μL with LPS (1 μg/mL) for 24 h. The concentration of nitrite was determined in culture supernatant. The data represented are means ± SD in triplicate cultures. Control is LPS-untreated total IHLs. $^*p < 0.05$.

TLR4-positive cells which have recognition mechanism to LPS in IHLs from non-treated and α-GalCer-treated wild-type mice. The mice were sacrificed at 0 (non-treatment), 6, 12 and 48 h after α-GalCer-treatment and IHLs were obtained. After IHLs were reacted with anti-CD16/CD32 antibody, they were stained with FITC-conjugated anti-F4/80 antibody and PE-conjugated anti-TLR4 antibody. Although IHLs from the mice at 12 h after treatment contained 14.6 ± 2.3% of F4/80 and TLR4 double-positive cells based on non-staining controls, those from the mice at 0, 6 and 48 h after treatment contained 6.6 ± 0.1%, 6.3 ± 0.8% and 7.9 ± 2.5% (Fig. 4A and B). Thus, IHLs from the mice at 12 h after treatment contained a higher proportion of F4/80 and TLR4 double-positive cells as compared with those from the mice at 0, 6 and 48 h after treatment. Also, F4/80 and TLR4 double-positive cell number from the mice at 12 h after treatment had increased as compared with those from the mice at 0, 6 and 48 h after treatment (Fig 4C).

Discussion

In the present study, we demonstrated that activation of Vα14 NKT cells by α-GalCer augments LPS-induced NO production in murine IHLs. Since such enhancement was not observed in IFN-γ −/− mice, it is suggested that IFN-γ secreted by Vα14 NKT cells activated with α-GalCer contributes to the augmentation of LPS-induced NO production in IHLs.

The liver plays an important role in the development of multiple organ failure (MOF) during sepsis. Whereas the gut is considered to be a main causative organ of MOF, the liver acts as the modulator of it [22]. Pathophysiologically, hypoperfusion of the gut during endotoxemia leads to disruption of the mucosal barrier following subsequent translocation of LPS to the portal vein [23,24]. Therefore, these reports agree that the liver is exposed to

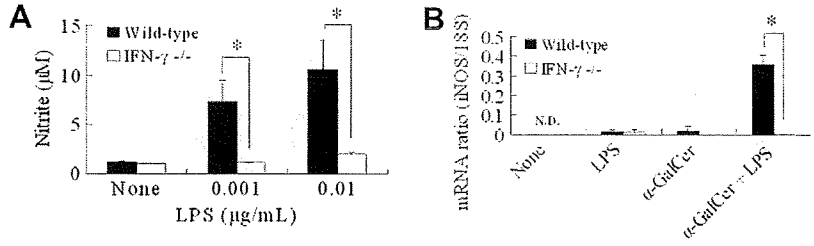

Fig. 2. Comparison of NO production and iNOS mRNA level between wild-type and IFN-γ KO mice with α-GalCer administration. IHLs were cultured at 1×10^5 cells/well with LPS. LPS concentration used was 0.001, 0.01 μg/mL in α-GalCer-treated-IHLs. The concentration of nitrite in the supernatant was determined 24 h after LPS stimulation (A). IHLs (1×10^5 cells/well) were cultured with LPS (α-GalCer treated-IHLs: 0.001 μg/mL, non-treated-IHLs: 10 μg/mL) for 24 h. The expression of iNOS mRNA was analyzed by real-time PCR and was determined based on 18 S mRNA (B). The data represented are means ± SD from 3 mice of each group. $^*p < 0.05$.

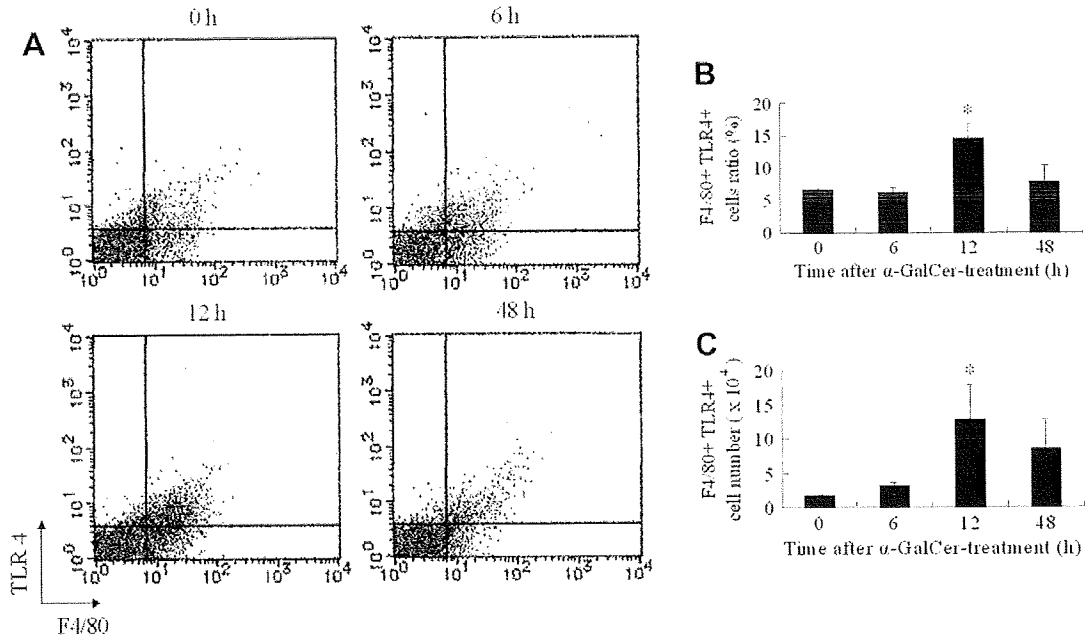

Fig. 4. Effect of α-GalCer on cell ratio and cell number of F4/80 and TLR4 double-positive cell in IHLs. The mice were sacrificed 0, 6, 12, and 48 h after α-GalCer-treatment and IHLs were obtained. After IHLs were reacted with anti-CD16/CD32 antibody, they were stained with anti-F4/80 (FITC, FL-1) and anti-TLR4 (PE, FL-2) antibody (A,B). And, F4/80 and TLR4 double-positive cell number was also measured (C). The data represented are means ± SD from 3 mice of each group. $^*p < 0.05$ vs. 0 h.

LPS stimulation and LPS-induced NO is then involved in the liver injury. In fact, several studies have examined the relationship between NO production and liver injury [10,14–18]. In the present study, LPS-induced NO production in IHLs from non-treated mice was not observed even in the presence of a high concentration of LPS (Fig. 1B). Thus, IHLs in their normal state may be not so susceptible to LPS, because sinusoidal cells including Kupffer cells are first exposed to LPS.

As a responsible molecule for NO-induced liver injury, peroxynitrite, a potent oxidant formed from NO and superoxide, has a higher reactivity than NO. Therefore, its toxicity to the liver may be considerably high. Peroxynitrite causes tyrosine nitration resulting in the formation of nitrotyrosine [6]. Actually, nitrotyrosine was detected at the sites of LPS-induced hepatic injury in D-galactosamine-sensitized mice, peroxynitrite appeared to cause hepatic injury [10], indicating that NO production strongly contributes to hepatic injury. Indeed, our results suggest that IHLs from α-GalCer-treated mice augmented LPS-induced NO production; in particular, CD11b-positive cells in IHLs produce LPS-induced NO (Fig. 3). Therefore, these data revealed that CD11b-positive cells were enhanced an ability to produce NO by α-GalCer. Previous reports indicated that IFN-γ production exhibit high value 4–12 h after α-GalCer-treatment [25,26] and our result demonstrated that IHLs from the mice at 12 h after α-GalCer-treatment highly produced NO. As shown in Fig. 1A, IHLs from the mice 0 and 48 h after α-GalCer-treatment did not produce NO. This data suggested that there is the correlation between LPS-induced NO production and IFN-γ production. It is common knowledge that IFN-γ is very important activator of iNOS. Since augmentation of NO production was not observed in Jα18 −/− mice and IFN-γ −/− mice, it was thought that IFN-γ from Vα14 NKT cell activated by α-GalCer is very important in this phenomenon. We also showed that the cell ratio and cell number of F4/80- and TLR4-positive cells which have recognition mechanism to LPS in IHLs rose by α-GalCer-treatment (Fig. 4). Consequently, it is assumed that both enhanced abilities of CD11b-positive cells and increased numbers of it is important in LPS-induced NO production.

The liver is highly susceptible to LPS in Vα14 NKT cell-activated state. It was previously reported that invariant NKT cells respond to the progressive liver damage caused by chronic hepatitis virus infection [27]. Moreover, invariant NKT cells have substantial effector potential, which characterizes the chronic liver damage, and also have the capacity to produce IL-4 and IL-13 besides IFN-γ. It is likely that the stage of liver disease depends on the activity of invariant NKT cells. Virus infection of the liver could potentially directly or indirectly provoke the activation of NKT cells, because NKT cells are abundant in the liver and a high amount of CD1d molecules are seen on hepatocytes [28]. On the other hand, CD1d-deficient mice have an increased susceptibility to encephalomyocarditis virus (EMCV), suggesting a physiological role of the CD1d molecule and/or CD1d-restricted T cells. Recently, Brion et al. examined the role of NKT cells during EMCV infection and found that, at 36 h after infection, the hepatic NKT cell population was dramatically reduced. This finding suggests an early activation of NKT cells, because stimulation of this population results in activation-induced cell death. It is thus considered that acute and chronic viral infections induce the activation of NKT cells. Our results that LPS-induced NO production is augmented by α-GalCer in IHLs raise the possibility that activation of NKT cells is involved in the liver injury via LPS and NO. In particular, chronic liver damage caused by hepatitis virus or autoimmune mechanisms may induce the activation of NKT cells in the liver, and the enhancement of LPS-induced NO production may contribute to liver injury.

In conclusion, we demonstrated that Vα14 NKT cells activated by alpha-galactosylceramide augment lipopolysaccharide-induced NO production in mouse intra-hepatic lymphocytes. We propose that while NKT cells have important roles in many infectious diseases and hepatic immunity, activation of NKT cells may elevate the sensitivity of the liver to NO via LPS.

Acknowledgments

We are grateful to Dr. T. Nakayama and Dr. M. Taniguchi for providing Vα14 NKT-deficient mice. We express our gratitude to

John Cole for reading our draft and giving us suggestions on language and style.

References

[1] M. Kronenberg, Toward an understanding of NKT cell biology: progress and paradoxes, Annu. Rev. Immunol. 23 (2005) 877–900.
[2] M. Kronenberg, L. Gapin, The unconventional lifestyle of NKT cells, Nat. Rev. Immunol. 2 (2002) 557–568.
[3] M. Taniguchi, M. Harada, S. Kojo, T. Nakayama, H. Wakao, The regulatory role of Valpha14 NKT cells in innate and acquired immune response, Annu. Rev. Immunol. 21 (2003) 483–513.
[4] R.B. Lorsbach, W.J. Murphy, C.J. Lowenstein, S.H. Snyder, S.W. Russell, Expression of the nitric oxide synthase gene in mouse macrophages activated for tumor cell killing. Molecular basis for the synergy between interferon-gamma and lipopolysaccharide, J. Biol. Chem. 268 (1993) 1908–1913.
[5] C. Nathan, Nitric oxide as a secretory product of mammalian cells, FASEB J. 6 (1992) 3051–3064.
[6] J.S. B eckman, W.H. K oppenol, Nitric oxide, superoxide, and peroxynitrite: the good, the bad, and ugly, Am. J. Physiol. 271 (1996) C1424–C1437.
[7] S. Dimmeler, A.M. Zeiher, Nitric oxide and apoptosis: another paradigm for the double-edged role of nitric oxide, Nitric Oxide 1 (1997) 275–281.
[8] K.D. Kroncke, K. Fehsel, V. Kolb-Bachofen, Nitric oxide: cytotoxicity versus cytoprotection—how, why, when, and where?, Nitric Oxide 1 (1997) 107–120
[9] S. Milano, F. Arcoleo, P. D'Agostino, E. Cillari, Intraperitoneal injection of tetracyclines protects mice from lethal endotoxemia downregulating inducible nitric oxide synthase in various organs and cytokine and nitrate secretion in blood, Antimicrob. Agents Chemother. 41 (1997) 117–121.
[10] A. Morikawa, Y. Kato, T. Sugiyama, N. Koide, D. Chakravortty, T. Yoshida, T. Yokochi, Role of nitric oxide in lipopolysaccharide-induced hepatic injury in D-galactosamine-sensitized mice as an experimental endotoxic shock model, Infect. Immun. 67 (1999) 1018–1024.
[11] T. Genovese, S. Cuzzocrea, R. Di Paola, M. Failla, E. Mazzon, M.A. Sortino, G. Frasca, E. Gili, N. Crimi, A.P. Caputi, C. Vancheri, Inhibition or knock out of inducible nitric oxide synthase result in resistance to bleomycin-induced lung injury, Respir. Res. 6 (2005) 58.
[12] P.L. Beck, Y. Li, J. Wong, C.W. Chen, C.M. Keenan, K.A. Sharkey, D.M. McCafferty, Inducible nitric oxide synthase from bone marrow-derived cells plays a critical role in regulating colonic inflammation, Gastroenterology 132 (2007) 1778–1790.
[13] H. Lu, B. Zhu, X.D. Xue, Role of neuronal nitric oxide synthase and inducible nitric oxide synthase in intestinal injury in neonatal rats, World J. Gastroenterol. 12 (2006) 4364–4368.
[14] S.E. McKim, E. Gabele, F. Isayama, J.C. Lambert, L.M. Tucker, M.D. Wheeler, H.D. Connor, R.P. Mason, M.A. Doll, D.W. Hein, G.E. Arteel, Inducible nitric oxide synthase is required in alcohol-induced liver injury: studies with knockout mice, Gastroenterology 125 (2003) 1834–1844.
[15] J. Menezes, C. Hierholzer, S.C. Watkins, V. Lyons, A.B. Peitzman, T.R. Billiar, D.J. Tweardy, B.G. Harbrecht, A novel nitric oxide scavenger decreases liver injury and improves survival after hemorrhagic shock, Am. J. Physiol. 277 (1999) G144–G151.
[16] G. Sass, K. Koerber, R. Bang, H. Guehring, G. Tiegs, Inducible nitric oxide synthase is critical for immune-mediated liver injury in mice, J. Clin. Invest. 107 (2001) 439–447.
[17] K. Koerber, G. Sass, A.K. Kiemer, A.M. Vollmar, G. Tiegs, In vivo regulation of inducible no synthase in immune-mediated liver injury in mice, Hepatology 36 (2002) 1061–1069.
[18] A. Mabuchi, T. Nagao, O. Koshio, T. Ishiwata, A. Yano, K. Suzuki, K. Yokomuro, A.M. Wheatley, Role of F4/80Mac-1 adherent non-parenchymal liver cells in concanavalin A-induced hepatic injury in mice, Hepatol. Res. 38 (2008) 1040–1049.
[19] R. Guler, M.L. Olleros, D. Vesin, R. Parapanov, C. Vesin, S. Kantengwa, L. Rubbia-Brandt, N. Mensi, A. Angelillo-Scherrer, E. Martinez-Soria, F. Tacchini-Cottier, I. Garcia, Inhibition of inducible nitric oxide synthase protects against liver injury induced by mycobacterial infection and endotoxins, J. Hepatol. 41 (2004) 773–781.
[20] H. Ito, N. Koide, A. Morikawa, F. Hassan, S. Islam, G. Tumurkhuu, I. Mori, T. Yoshida, S. Kakumu, H. Moriwaki, T. Yokochi, Augmentation of lipopolysaccharide-induced nitric oxide production by alpha-galactosylceramide in mouse peritoneal cells, J. Endotoxin Res. 11 (2005) 213–219.
[21] L.C. Green, D.A. Wagner, J. Glogowski, P.L. Skipper, J.S. Wishnok, S.R. Tannenbaum, Analysis of nitrate, nitrite, and [15N]nitrate in biological fluids, Anal. Biochem. 126 (1982) 131–138.
[22] G.M. Matuschak, J.E. Rinaldo, Organ interactions in the adult respiratory distress syndrome during sepsis, role of the liver in host defense, Chest 94 (1988) 400–406.
[23] P. Baron, L.D. Traber, D.L. Traber, T. Nguyen, M. Hollyoak, J.P. Heggers, D.N. Herndon, Gut failure and translocation following burn and sepsis, J. Surg. Res. 57 (1994) 197–204.
[24] H. Schmidt, A. Secchi, R. Wellmann, A. Bach, H. Bohrer, M.M. Gebhard, E. Martin, Effect of endotoxemia on intestinal villus microcirculation in rats, J. Surg. Res. 61 (1996) 521–526.
[25] H. Kitamura, K. Iwakabe, T. Yahata, S. Nishimura, A. Ohta, Y. Ohmi, M. Sato, K. Takeda, K. Okumura, L. Van Kaer, T. Kawano, M. Taniguchi, T. Nishimura, The natural killer T (NKT) cell ligand alpha-galactosylceramide demonstrates its immunopotentiating effect by inducing interleukin (IL)-12 production by dendritic cells and IL-12 receptor expression on NKT cells, J. Exp. Med. 189 (1999) 1121–1128.
[26] H. Kitamura, A. Ohta, M. Sekimoto, M. Sato, K. Iwakabe, M. Nakui, T. Yahata, H. Meng, T. Koda, S. Nishimura, T. Kawano, M. Taniguchi, T. Nishimura, Alpha-galactosylceramide induces early B-cell activation through IL-4 production by NKT cells, Cell. Immunol. 199 (2000) 37–42.
[27] C. de Lalla, G. Galli, L. Aldrighetti, R. Romeo, M. Mariani, A. Monno, S. Nuti, M. Colombo, F. Callea, S.A. Porcelli, P. Panina-Bordignon, S. Abrignani, G. Casorati, P. Dellabona, Production of profibrotic cytokines by invariant NKT cells characterizes cirrhosis progression in chronic viral hepatitis, J. Immunol. 173 (2004) 1417–1425.
[28] C.A. Biron, L. Brossay, NK cells and NKT cells in innate defense against viral infections, Curr. Opin. Immunol. 13 (2001) 458–464.

BioSystems 99 (2010) 70–78

Contents lists available at ScienceDirect

BioSystems

journal homepage: www.elsevier.com/locate/biosystems

Reproducibility and usability of chronic virus infection model using agent-based simulation; comparing with a mathematical model

Jun Itakura[a,*], Masayuki Kurosaki[a], Yoshie Itakura[a], Sinya Maekawa[b], Yasuhiro Asahina[a], Namiki Izumi[a], Nobuyuki Enomoto[b]

[a] Division of Gastroenterology and Hepatology, Musashino Red Cross Hospital, 1-26-1 Kyonan-cho, Musashino-shi, Tokyo 180-8610, Japan
[b] First Department of Internal Medicine, Faculty of Medicine, University of Yamanashi, 1110, Shimogatou, Chuou-shi, Yamanashi 409-3898, Japan

ARTICLE INFO

Article history:
Received 30 June 2009
Received in revised form 27 August 2009
Accepted 6 September 2009

Keywords:
Agent-based model
Virus infectious disease

ABSTRACT

We created agent-based models that visually simulate conditions of chronic viral infections using two software. The results from two models were consistent, when they have same parameters during the actual simulation. The simulation results comprise a transient phase and an equilibrium phase, and unlike the mathematical model, virus count transit smoothly to the equilibrium phase without overshooting which correlates with actual biology in vivo of certain viruses. We investigated the effects caused by varying all the parameters included in concept; increasing virus lifespan, uninfected cell lifespan, uninfected cell regeneration rate, virus production count from infected cells, and infection rate had positive effects to the virus count during the equilibrium period, whereas increasing the latent period, the lifespan-shortening ratio for infected cells, and the cell cycle speed had negative effects. Virus count at the start did not influence the equilibrium conditions, but it influenced the infection development rate. The space size had no intrinsic effect on the equilibrium period, but virus count maximized when the virus moving speed was twice the space size. These agent-based simulation models reproducibly provide a visual representation of the disease, and enable a simulation that encompasses parameters those are difficult to account for in a mathematical model.

1. Introduction

All viruses need hosts as a basis for their life. When a virus enters the host body, it invades cells and uses both its own enzymes and those of the host cells to replicate. Host cells infected by viruses launch a self-defense system known as the innate immune system (See and Wark, 2008; Naniche, 2009), which inhibits viral replication and uses the human leukocyte antigen system and cytokines to elicit an immune response. Immune cells that have received signals from host cells activate other immune cells, neutralize viruses in the serum by means of antibodies, and prevent the virus from replicating and proliferating by destroying or curing host cells. Viral infection is a disorder based on the interactions between viruses and cells.

The power relationship between these agents changes along with the progression of the disease. In the very early stages of infection, as the host defense mechanisms are immature, the virus has the ability to overwhelm the host cells, actively replicate, and proliferate. Subsequently, as the capacity of the immune system improves, the speed of viral proliferation drops and the virus count reaches a peak. Infected host cells begin to be disrupted by the immune system or virus particles, and symptoms appear as a result. If the immune system is stronger than the virus, then the viral counts decline, and, in transient viral disorders, the virus is finally eliminated and the host recovers. In chronic viral disorders, however, the power relationship between the virus and host cells reaches equilibrium, and a long-term power balance is maintained with the virus count reaching a plateau.

Mathematical models have been proposed to study the dynamics of such viral disorders, and are regarded as being of value in understanding this phenomenon (Ho et al., 1995; Nowak et al., 1996; Neumann et al., 1998). However, these models are difficult to understand for clinicians, and their applicability is somewhat limited in everyday practice. In clinical research, measurements of viral dynamics in patients for short duration have been made for human

Abbreviations: HIV, human immunodeficiency virus; HBV, hepatitis B virus; HCV, hepatitis C virus.

* Corresponding author. Tel.: +81 422 32 3111; fax: +81 422 32 9551.
E-mail address: jitakura@musashino.jrc.or.jp (J. Itakura).

0303-2647/$ – see front matter © 2009 Elsevier Ireland Ltd. All rights reserved.
doi:10.1016/j.biosystems.2009.09.001

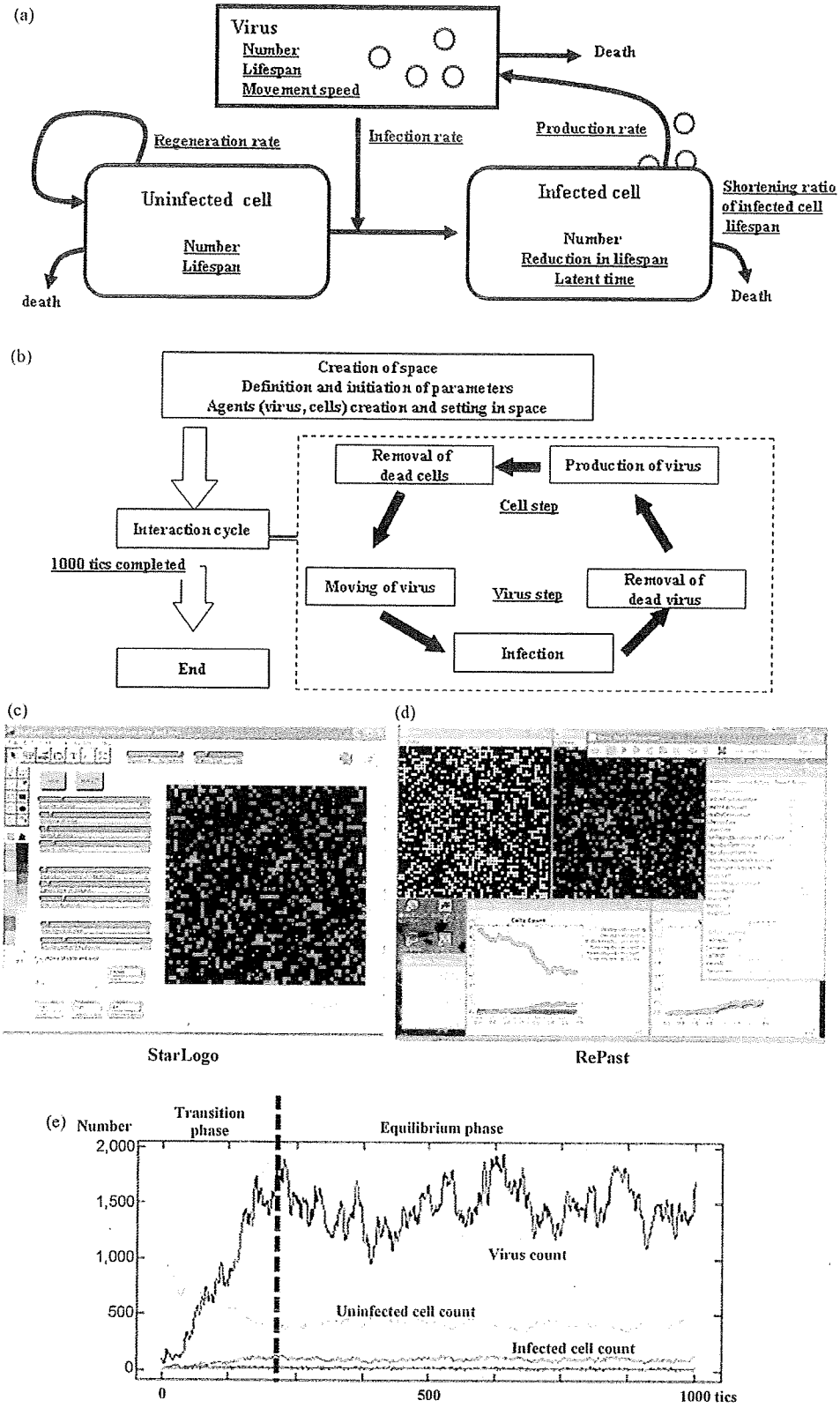

Fig. 1. Simulation design and an example of simulation results. (a) Model concept. Viruses, uninfected cells, and infected cells were treated as agents, and parameters were set for each of these and for interactions between agents (underlined). (b) Flowchart of the program. After preparing the simulation, we entered the interaction cycle, in which virus steps (such as movement) and cell steps were repeated. One cycle was counted as 1 tic, and the simulation concluded after 1000 tics. (c and d) Simulation screen using (c) StarLogo and (d) RePast. Yellow circles are viruses, green squares are uninfected cells, and orange and red indicate infected cells, with orange indicating the latent period. In StarLogo, all the agents are shown on the same screen, but in RePast, viruses and cells are shown in separate windows. (e) Example of a simulation chart in StarLogo. After the start of simulation the virus count and infected cell count increase while the uninfected cell count decreases, with equilibrium state reached after a certain number of tics.

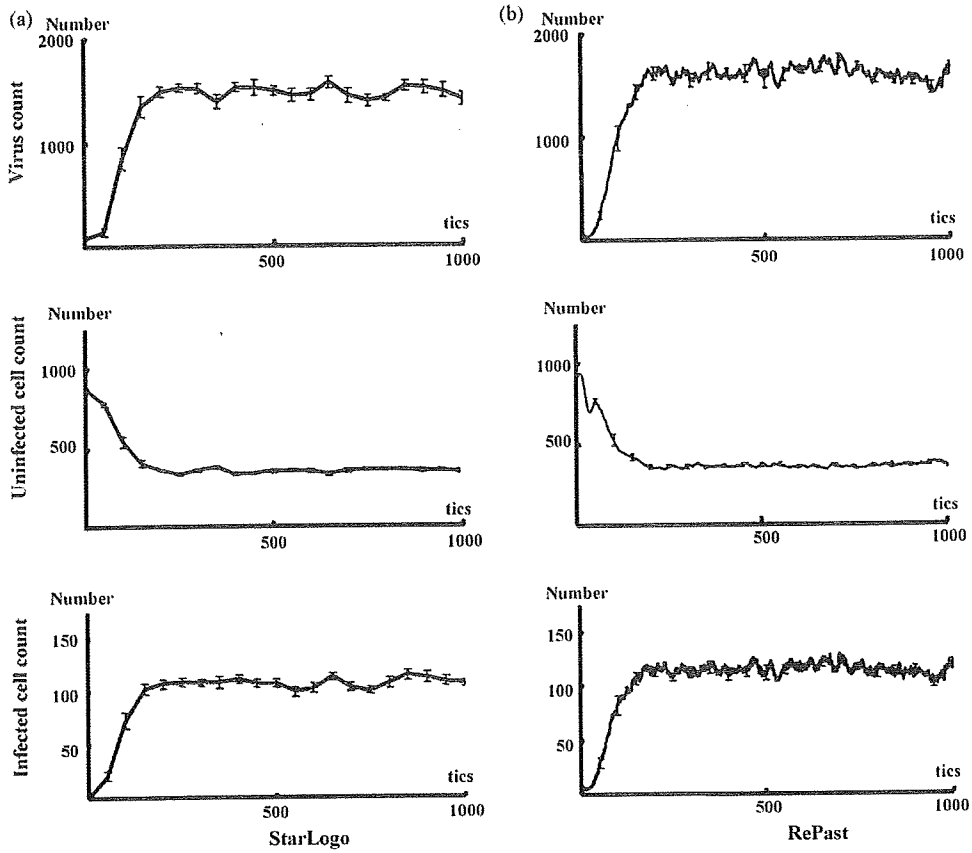

Fig. 2. Comparison of simulation results in (a) StarLogo and (b) RePast. The results were consistent when the parameters were made consistent. (Virus count [average ± SD]: StarLogo 1458.03 ± 173.1, RePast 1462.71 ± 178.8, $p = 0.94$. Uninfected cell count: 364.24 ± 30.4, 368.11 ± 33.4, $p = 0.83$. Infected cell count: 105.73 ± 13.0, 107.74 ± 13.0, $p = 0.24$. Unpaired Student's t-test.) Parameter values were set as follows: initial virus count, 100; uninfected cell count, 880; infected cell count, 0; virus speed of movement, 5 grids/tic; infection rate, 10%; uninfected cell regeneration rate, 1%; latent period, 3 tics; and virus reproduction rate, 5/cells/tic. The following parameter settings were taken from actual measurements: virus lifespan, 4.5 tics; uninfected cell lifespan, 49.8 tics; and infected cell lifespan, 6.7 tics.

immunodeficiency virus (HIV) (Ho et al., 1995), hepatitis B virus (HBV) (Nowak et al., 1996) and hepatitis C virus (HCV) (Neumann et al., 1998), and research is also underway on a range of models based on animal experiments and cell culture systems. As chronic viral disorders persist over long periods of time complete follow-up of viral dynamics is difficult. Furthermore, limitations of items that can be measured, such as the difficulty of measuring whole numbers of host cells, make it extremely difficult to investigate their consistency in mathematical models.

The recent ascend of dynamic-models owes much to advances in computers. Computer performance has improved markedly in recent years, not only in terms of their calculating capacity but also with regard to image displays, and models that offer a visual representation of viral disorders are now being reported (Gilbert and Bankes, 2002; Duca et al., 2007; Shapiro et al., 2008; Castiglione et al., 2007). One advantage of such visual models is that by providing a visual representation, they make understanding the disease status easy. Another benefit is that they enable parameters to be identified that are hidden as background noise in mathematical models. However, these models have some problems; it is difficult to prove the reproducibility of the simulation results derived from different languages or libraries, difficult to prove the validity of the model's concepts, and difficult to prove that the simulation results accurately reflect the reality. In this study, we created agent-based computer models that visually simulate the conditions of chronic viral infections using two software. The reproducibility of two agent-based computer models and the differences between agent-based models and the mathematical model were analyzed. This agent-based model enabled us to investigate how each parameter included in the concept affects the conditions of chronic viral infections.

2. Methods

2.1. Selection of Software

In this study, we used two different types of softwares: StarLogo version 2.0 (http://education.mit.edu/starlogo/) supplied by MIT Media Laboratory and Recursive Porous Agent Simulation Toolkit (RePast-3.0, http://repast.sourceforge.net/) supplied by the Argonne National Laboratory. StarLogo uses Logo, one of the simplest programming languages, and has a fixed graphical user interface. RePast is a library that uses Java, another programming language, which also has a fixed graphical user interface.

Logo is an assembly language, and StarLogo carries out processing sequentially. Java is an object-oriented language, and RePast has a faster processing speed than StarLogo. In addition, StarLogo has a number of stipulations to simplify simulations, such as parameters can only be set up to five decimal places and the simulation space is also fixed as 51 × 51 square grids. RePast, on the other hand, has fewer such restrictions. Thus, it offers a higher degree of freedom in program settings than StarLogo. Taking simulation space as an example, in spite of the restrictions imposed by the underlying operating system's image display system, any number of grids can be set and a hexagonal grid could also be chosen rather than a square one. However, users must stipulate and set all parameters themselves. This means that they must first declare the shape of the grid and the number of grids they will use to fill the simulation space. Java is also more difficult to learn than Logo, and debugging and correcting the program is also more difficult. Thus, it is difficult to judge whether or not the results agree with the planned simulation.

In effect, these two different types of softwares are polar opposites. It is simple to start a simulation in StarLogo, but producing results takes time and it is difficult to carry out more complex simulations. In RePast it is difficult to compose the program and judge whether or not the planned study has actually been achieved, but the

simulation itself takes only a short time to complete and there are lesser restrictions in the construction of a simulation model.

2.2. Concept for Modeling

We applied the basic virus–host interaction mathematical model to the agent-based simulation system with slight modifications. The mathematical model was used to describe the dynamics of HIV (Ho et al., 1995), HBV (Nowak et al., 1996), and HCV (Neumann et al., 1998) and the only agents involved were host cells and viruses, without the inclusion of immune cells. The effects of the immune system are expressed by varying parameters such as lifespan of host cells and viruses.

Fig. 1a illustrates the study concept. Viruses have the ability to infect healthy host cells (uninfected cells) and the infected cells produce new viruses. Both cells and viruses have definite lifespans, and the lifespan of infected cells is usually shorter than that of uninfected cells. Uninfected cells automatically regenerate within the space, whereas infected cells only arise due to infection of uninfected cells. Viruses also lack the ability to regenerate themselves and are only produced from infected cells.

2.3. Parameter Settings

In the present study, as the StarLogo settings are circumscribed, we limited the simulation space to 51 × 51 square grids. However, we made an exception here while investigating the effects of size of space on the simulation results. The numbers of viruses, uninfected cells, and infected cells could only be set before the start of the simulation. As described in the later, our simulation ran in cycles, with 1 cycle defined as 1 tic.

In mathematical simulation models, the death rate is required as a parameter. However, in our program we set lifespans for viruses and uninfected cells. These lifespans were not uniform, but were set to have a deviation of about 10%. The lifespan of cells was shortened by infection with ratio decided beforehand.

The infection ratio was meaningful only when an infected cell and a virus coincidentally occupied the same grid, and this was used to calculate the probability of the infection occurring in that situation. The virus production rate was set as the number of viruses produced by an infected cell during 1 tic. Infected cells could be set as a parameter indicating the latent period between the time of virus infection and the time of virus replication.

In order to emulate the tissue repair capacity, we set uninfected cell regeneration rate such that grids without any cells had a specified probability of producing uninfected cells on top of themselves. As a result, the more the cell count declined within a space the more regenerated uninfected cells were produced, whereas the number of regenerated cells declined as cell count increased.

The number of grids through which a virus could move in 1 tic was set as the speed of movement, and the direction of movement was set within a range of 90° toward the top of the simulation space. The program used a circulatory method of movement; when a virus arrived at the top of the space, it was translocated to the bottom, and moved again toward the top. Cells were fixed on the grid.

2.4. Simulation Flowchart

Fig. 1b shows a flowchart of the program. First, the simulation space was produced, after which each parameter was defined and the initial settings were made. Next the agents – viruses and uninfected and infected cells – were produced. The simulation cycle was as follows. Viruses moved to a new grid, and if an uninfected cell was present, this was infected with a probability based on the infection rate. The lifespan of the virus decreased, and viruses that had completed their lifespan and those that had caused an infection were removed from the space. Infected cells produced new viruses, the lifespans of both uninfected and infected cells decreased. Then, cells that had completed their lifespan were eliminated and a new cycle began. The program was set such that the simulation ended after this cycle had repeated 1000 times. This meant that one simulation was complete after 1000 tics.

2.5. Data Collection

The RePast model was programmed such that data for each tic was saved automatically as a text file at the end of the simulation. This text file could be opened by a database software. The StarLogo model was programmed to stop the simulation and collect data after every 50 tics.

2.6. Mathematical Model

In order to compare the results of this agent-based simulation, we used a viral infection mathematical model, which we improved as follows.

$$\frac{dT}{dt} = s[2601 - (T+I)] - dT - bVT \quad (1)$$

$$\frac{dI}{dt} = bVT - dI \quad (2)$$

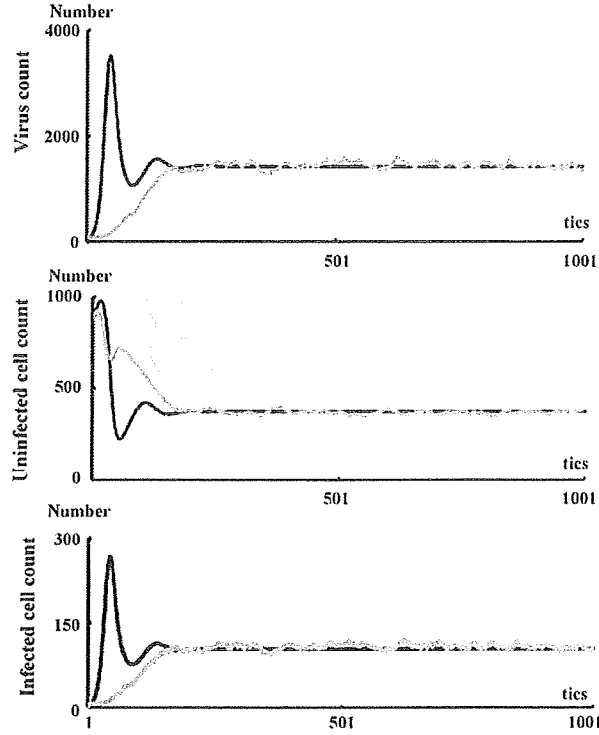

Fig. 3. Comparison of results of agent-based simulation and mathematical simulation. Both sets of results were consistent for the equilibrium phase, but differed in the shift in transition phase. Black line: mathematical model; grey line: results of simulation in RePast. Parameter values were set as follows: initial virus count, 100; uninfected cell count, 880; infected cell count, 0; virus speed of movement, 5 grids/tic; infection rate, 10%; uninfected cell regeneration rate, 1%; latent period, 3 tics; virus reproduction rate, 5/cells/tic; virus lifespan, 10 tics; uninfected cell lifespan, 50 tics; and cell lifespan-shortening ratio as a result of infection, 69%.

$$\frac{dV}{dt} = pI - cV \quad (3)$$

where, T is the uninfected cell count, I is the infected cell count, and V is the virus count. Uninfected cells are supplied to the space with a probability $s[2601 - (T+I)]$, as the number of grids in this agent-based simulation model was 2601 (51 × 51). The death rate of uninfected cells is d, the death rate of infected cells is δ, and the death rate of viruses is c. The infection rate is indicated by β. Viruses are released from infected cells at a probability p.

2.7. Statistical Analysis

Statistical analyses were performed by statistical tests using the program StatView 5.0 (SAS Institute Inc.). All tests of significance were two-tailed, with p values of <0.05 considered to be significant.

3. Results

3.1. Reproducibility of Chronic Viral Infection Disease Models Using Agent-based Simulation Methods

We constructed the chronic viral infection model with StarLogo library. Fig. 1c shows the simulation screen, and Fig. 1e shows one sample result. Immediately after the start of the simulation, the virus count temporarily dropped in accordance with the onset of an infection. Subsequently, the virus count started to increase with an increase in the infected cells and a decrease in the uninfected cells. After a certain number of tics (around 300 in this example), although the virus count, infected cell count, and uninfected cell count had some fluctuation, an equilibrium state was reached. We use the following descriptive terms in this paper: the transient phase is the period during which virus growth peaks, and the equilibrium phase is the period during which an equilibrium state is

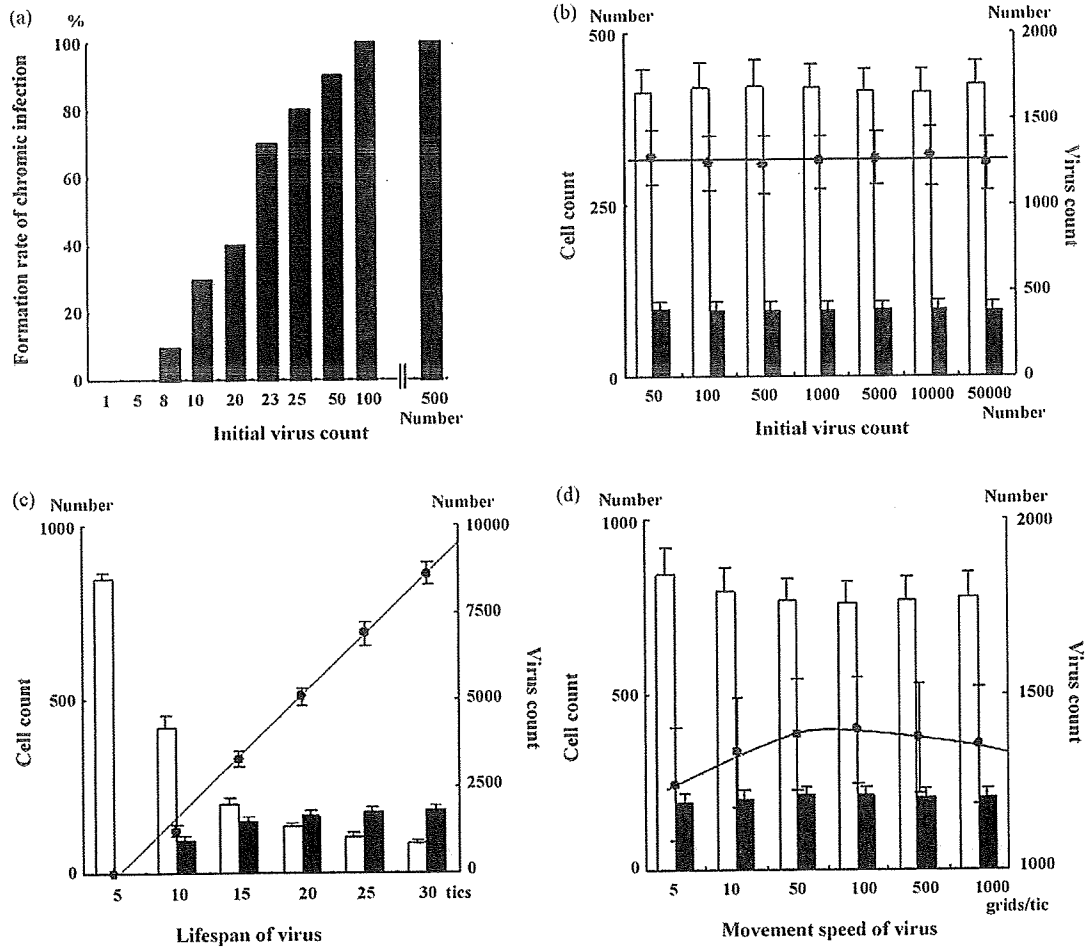

Fig. 4. Effects of changes in viral parameters. (a) The higher the initial virus count, the greater is the increase in the rate of formation of chronic infection, but (b) there was no effect on the conditions in the equilibrium phase. (c) Extending the virus lifespan increased the virus count. (d) Increasing the speed of virus movement to 100 grids/tic increased the virus count, but increasing it to 500 grids/tic had the opposite effect, with a slight declining trend. (a) Black bars: number of infections produced; (b–d) black circles: virus count; line: virus count approximation curve; white bars: uninfected cell count; black bars: infected cell count.

established. When the simulation was performed multiple times, the features described above were maintained, and the average values for virus, infected cell, and uninfected cell counts during the equilibrium state were all consistent.

Fig. 1d shows the simulation screen of the RePast. When we attempted setting all the initial parameters to the same values as those in the StarLogo, the results were not consistent. When we recalculated the parameters from the simulation results, in RePast, the parameters were largely maintained at the levels of the settings, but in StarLogo, the lifespans of both cell types became shorter than the settings while the simulation was in progress. We made the results of both simulations consistent by using the same parameters during the actual simulation (Fig. 2a and b).

3.2. Comparison Between Agent-based Simulation Models and Mathematical Simulation Model

We investigated whether the results of a chronic viral infection disease model produced by RePast would be consistent with the results of a mathematical model. For the mathematical model, we carried out an approximate integration using a four-dimensional Runge–Kutta method to ensure that the uninfected cell count and infected cell count would be in the same class. Parameters were always fixed as constant between simulations. The simulation results were consistent for the equilibrium phase, but transitions in virus count during the transient phase varied, with a shift to equilibrium state following two overshoots in the mathematical model, but a monotonic increase following a logistic curve in the agent-based model (Fig. 3). In the mathematical model, when the equilibrium condition was calculated with $dT/dt = dI/dt = dV/dt = 0$, the equilibrium-phase virus count, uninfected cell count, and infected cell count were very similar to those of the agent-based model (virus count: mathematical model 371.8/space, agent-based model 371.1 ± 32.4/space [average ± SD]; uninfected cell count: mathematical model 1605/space, agent-based model 1454 ± 194/space; infected cell count: mathematical model 115.9/space, agent-based model 108.3 ± 14.2/space).

3.3. Usability of the Models; Effect of Changing Parameters

We investigated the changes in the equilibrium phase brought about by changing each parameter. All the investigations below were carried out by using RePast, and we used the average values from ten simulations.

3.4. Viral Parameters

The lower the virus counts at the beginning of the simulation, the lower the probability of a chronic infection (Fig. 4a). However, the initial virus count did not have any effect on the equilibrium

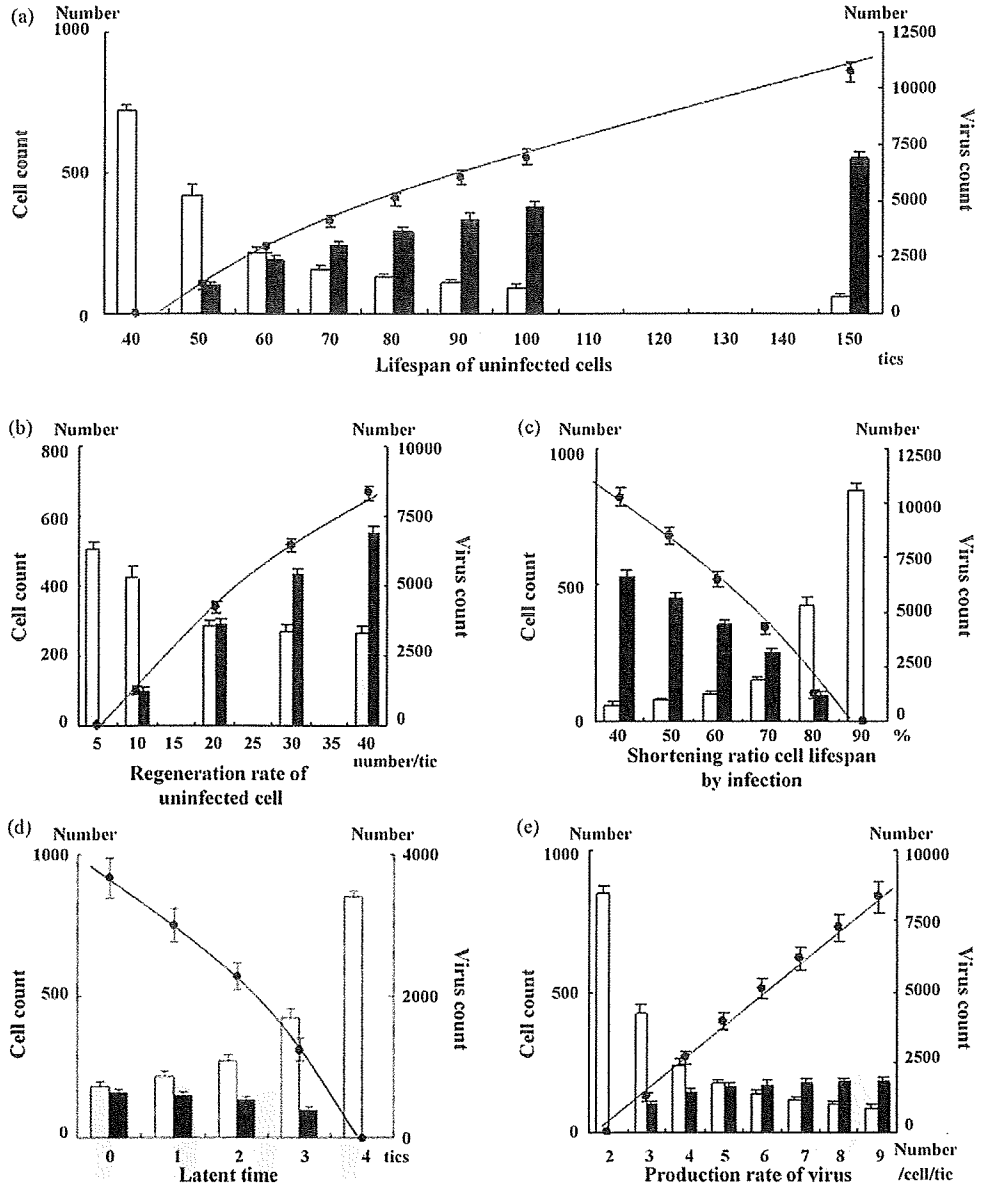

Fig. 5. Effects of changes in cell parameters. (a) Extending the uninfected cell lifespan and (b) increasing the uninfected cell regeneration rate increased the virus count. (c) Raising the lifespan-shortening ratio as a result of infection shortened the lifespan of infected cells, thereby decreasing the virus count. (d) Extending the latent period shortened the period of virus production from infected cells, thereby decreasing the virus count. (e) Increasing the virus production count resulted in a linear increase in equilibrium-phase virus count. Black circles: virus count; line: virus count approximation curve; white bars: uninfected cell count; black bars: infected cell count.

phase itself (Fig. 4b). Extending the lifespan of viruses resulted in a linear increase in equilibrium-phase virus count (Fig. 4c). Although the infected cell count increased, the rate of increase gradually declined. Changing the speed of viral movement resulted in the equilibrium-phase virus count to eventually decline after 100 grids/tic was reached, allowing movement over an area twice the size of the simulation space (Fig. 4d).

3.5. Uninfected Cell Parameters

Extending the lifespan of uninfected cells led to an increased virus count during the equilibrium phase (Fig. 5a). Increasing the uninfected cell regeneration rate also contributed to increased equilibrium-phase virus count (Fig. 5b). In both the cases, the increases in virus count and infected cell count were not linear, but showed a tendency for the rate of increase to decline gradually.

3.6. Infected Cell Parameters

We carried out an investigation of the effects of variation in the lifespan-shortening ratio on the virus count on the assumption that cell lifespan is shortened by infection. When this ratio was increased, the virus count decreased (Fig. 5c). An extended latent period was also related to a decreased virus count (Fig. 5d). However, the virus production from infected cells led to a linear increase in the virus count (Fig. 5e).

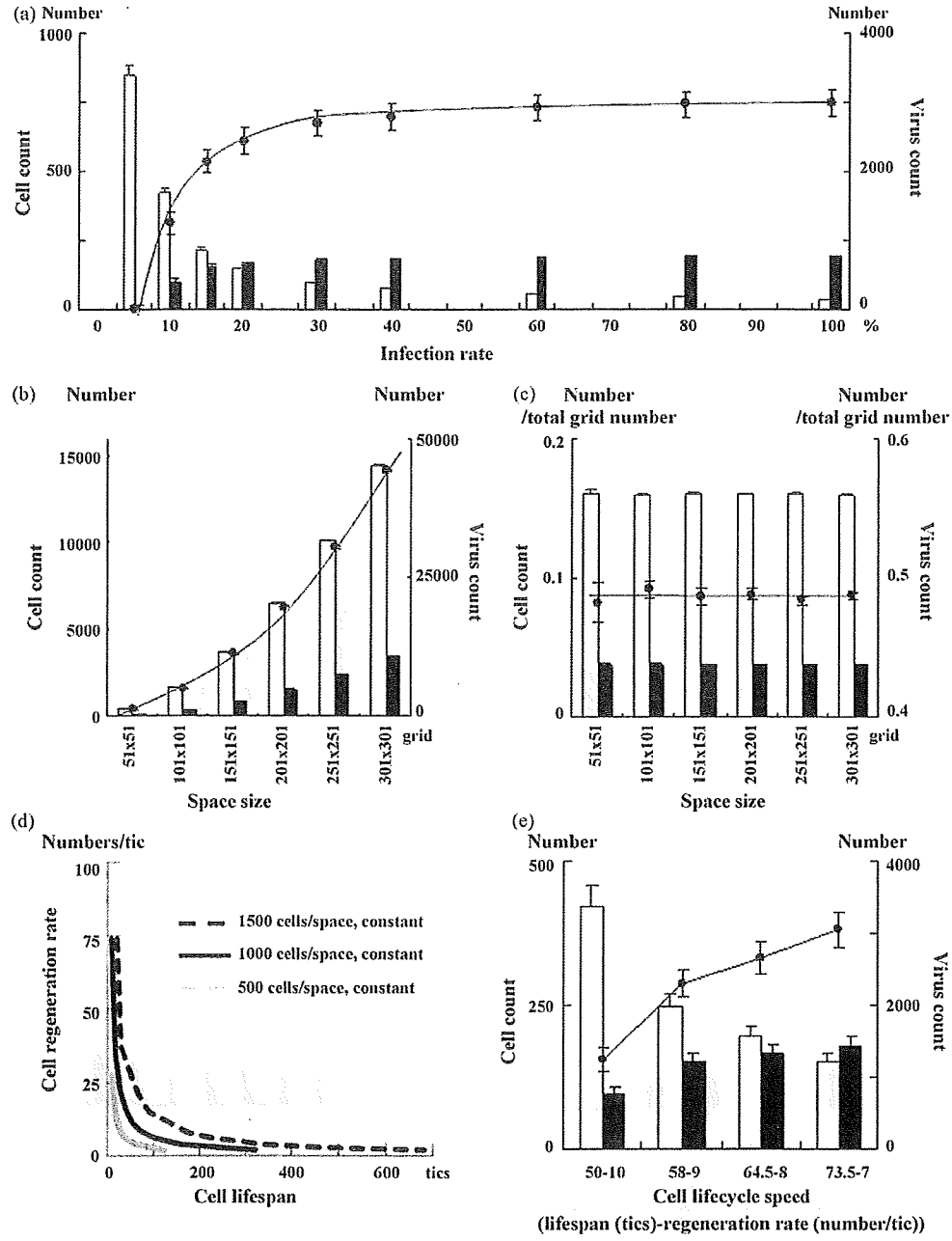

Fig. 6. (a) Increasing the infection rate increased the virus count in equilibrium periods, but the virus count did not change at infection rates of 30% or more. (b) The size of the simulation space increased not only virus count but also the cell count; however, (c) when virus and cell counts were divided by the total number of grids in the space, they were constant for all space sizes. (d) Changing the lifespan and regeneration rate of uninfected cells in opposite directions at the same time makes it possible to change only the cell cycle speed without altering the uninfected cell count. (e) When the cell cycle speed was reduced, the virus count increased toward the right of the graph. This may be because the effect of extending the lifespan of cells exceeds that of reducing their regeneration rate. (a–c and e) Black circles: virus count; line: virus count approximation curve; white bars: uninfected cell count; black bars: infected cell count.

3.7. Infection Rate and Space Size

Increasing the infection rate caused an increase in the virus count, but the change was minimal at an infection rate of 30% or more. The same results were seen for infected cell count, but a decrease in uninfected cell count resulted in a tendency for the infection rate to decrease by up to 60% (Fig. 6a).

The larger the space, higher the increase in both virus and cell counts (Fig. 6b). This increase was proportional to space size, however, when virus and cell counts were divided by the total number of grids in the space they were all constant (Fig. 6c).

3.8. Cell Cycle Speeds

Running a simulation with the initial virus count set to zero enables only the equilibrium condition for uninfected cells to be simulated. Changing the lifespan and regeneration rate of uninfected cells in opposite directions at the same time makes it possible

to change the cell cycle speed without altering the uninfected cell count (Fig. 6d). We used this technique to investigate how changing the cell cycle speed affected the equilibrium phase. Fig. 6e shows the results. Cell lifespan increases while the cell cycle speed declines. The equilibrium virus count increased in accordance with slower cell cycle speeds.

4. Discussion

In this study, we investigated the models using two agent-based simulation methods to program a simple virus–host chronic infection model. The same model written in two different programming language systems displayed the same results. The transient phase was unlike that seen in a mathematical simulation with no overshoot in virus count, but rather a smooth transition to the equilibrium phase. The virus count at the start of the simulation only had effect on the rate of infection development. Increases in virus lifespan, uninfected cell lifespan, uninfected cell regeneration rate, virus production count from infected cells, and infection rate all led to increased equilibrium-phase virus count. Rises in the infected cell lifespan-shortening ratio, latent period, and cell cycle speed decreased the equilibrium-phase virus count. The size of the space itself had no innate effect on the equilibrium phase, but a speed of movement of the virus that was twice the size of the space produced the maximum virus count.

Reproducibility is the basis for all scientific study, but there are many problems to prove it in computer simulations, such as programming bugs. As agent-based simulation deals with numerous agents individually, it requires vast amounts of calculations. Accumulation of very small change of values leads to large differences of results. In this study, we investigated two programs based on two programming languages to confirm the reproducibility of our simulation results in different programming languages. The results of two simulations were consistent, but in StarLogo, the lifespan parameters had a tendency to be lower than when they were set while simulations were actually in progress. This may be because the number of digits used in calculations was different between the two programs. RePast performs calculations to at least eight decimal places. In StarLogo, the library settings only enable settings to be made up to five decimal places. It is probable that these small differences accumulate during repeated calculations and are reflected in the simulation. Ultimately, we confirmed that the differences in results obtained by using different libraries and programming languages were not innate and by making the parameters consistent during simulation, consistent results were obtained.

Mathematical models using formulae for HIV therapy was published in 1994, the method has since been applied to HBV and HCV (Ho et al., 1995; Nowak et al., 1996; Neumann et al., 1998), and they were thought to be good reflections of the reality. In the mathematical model, viruses and cells are conceived as individuals in the concept itself, but both of them are perceived *en masse* when calculations are performed. However a feature of the agent-based simulation is that it deals with individual viruses and cells as separate agents. By moving each agent individually, it probes the factors influencing overall shifts from the micro viewpoint. When the space is viewed as a whole, it is possible to watch on the screen the collective movement of groups of agents. Recently, models that provide a visual representation of Epstein-Barr virus and HIV infection have been reported, both of which are useful for an instinctive and intuitive understanding (Duca et al., 2007; Shapiro et al., 2008; Castiglione et al., 2007).

In agent-based simulation model, virus count transit smoothly to the equilibrium phase. On the other hand, virus counts overshoot during transient phase in mathematical model. We think this difference is derived from technicality of different modeling. The difference in concepts between mathematical models and agent-based models is the space. The mathematical model has no space in concept, but agents move across the space in the agent-based model. In agent-based models, the densities of virus and cells change overtime especially in the transition phase because of the limited space. These changes of the densities of virus and cells lead to the dynamic change of the encounter rate of viruses and cells. The mathematical model does not make such concept of the density; the encounter rate is constant. This may be the reason for the difference between two models in the transition phase. Since no overshoot of virus counts in transient phase had been reported from in vivo studies of hepatitis C virus and simian immunodeficiency virus (Dahari et al., 2005; Nowak et al., 1997), agent-based model correlates with actual biology in vivo at least for these viruses. The increase of initial virus count at the start of simulation correlates with higher encounter rate of viruses and cells which make the linear increasing of infection forming rate. Mathematical model can only express the infection formation rate as "infected or not".

The importance of viral passing speed in the agent-based model is also explained by the "space". Although the virus actually moves through the blood stream in our body and virus could not decide their moving speeds by themselves, there is most appropriate speed for virus to meet the cells on the simulation space by the highest probability. The effect of cell cycle speed should be mentioned by another affection of the space. A fast cell cycle speed means that the lifespan of uninfected cells is short. Then fast cell cycle speed leads to the short lifespan of infected cells. A higher regeneration rate for uninfected cells results in a higher rate of infection among uninfected cells by viruses, but in situations where viruses and cells are dispersed around the space this is ineffective in increasing the infection rate, as the latter depends on the probability that they will encounter one another. As a result, the infected cell count decreases during the equilibrium phase, as does the virus count.

In this study, we confirmed the reproducibility and usability of agent-based models in expressing the interaction between viruses and cells. A feature of this simulation system is that it uses the concept of space as actual space, which means that the existence of the space becomes an additional controlling factor on the simulation results. This is a concept that is absent from mathematical models. The reality is that we have a spatial existence, and an advantage of the agent-based simulation system is the fact that it accounts for the space. Another feature of the simulation system is that it enables the condition to be perceived in visual terms, making it easy to understand. However it may be affected by computer performance and by the limitations of programming languages or the program itself, this system may offer a powerful tool for the future analysis of real virus–host interaction disease.

Conflict of interest

No conflicts of interest exist for all authors.

References

Castiglione, F., Pappalardo, F., Bernaschi, M., Motta, S., 2007. Optimization of HAART with genetic algorithms and agent-based models of HIV infection. Bioinformatics 23, 3350–3355, doi:10.1093/bioinformatics/btm408.

Dahari, H., Major, M., Zhang, X., Mihalik, K., Rice, C.M., Perelson, A.S., Feinstone, S.M., Neumann, A.U., 2005. Mathematical modeling of primary hepatitis c infection: noncytolytic clearance and early blockage of virion production. Gastroenterology 128, 1056–1066, doi:10.1053/j.gastro.2005.01.049.

Duca, K.A., Shapiro, M., Delgado-Eckert, E., Hadinoto, V., Jarrah, A.S., Laubenbacher, R., Lee, K., Luzuriaga, K., Polys, N.F., Thorley-Lawson, D.A., 2007. A virtual look at Epstein-Barr virus infection: biological interpretations. PLoS Pathog. 3, 1388–1400, doi:10.1371/journal.ppat.0030137.

Gilbert, N., Bankes, S., 2002. Platforms and methods for agent-based modelling. Proc. Natl. Acad. Sci. U.S.A. 99 (Suppl. 3), 7197–7198.

Ho, D.D., Neumann, A.U., Perelson, A.S., Chen, W., Leonard, J.M., Markowitz, M., 1995. Rapid turnover of plasma virions and CD4 lymphocytes in HIV-1 infection. Nature 373, 123–126, doi:10.1038/373123a0.

Naniche, D., 2009. Human immunology of measles virus infection. Curr. Top. Microbiol. Immunol. 330, 151–171.

Neumann, A.U., Lam, N.P., Dahari, H., Gretch, D.R., Wiley, T.E., Layden, T.J., Perelson, A.S., 1998. Hepatitis C viral dynamics in vivo and the antiviral efficacy of interferon-alpha therapy. Science 282, 103–107, doi:10.1126/science.282.5386.103.

Nowak, M.A., Bonhoeffer, S., Hill, A.M., Boehme, R., Thomas, H.C., McDade, H., 1996. Viral dynamics in hepatitis B virus infection. Proc. Natl. Acad. Sci. U.S.A. 93, 4398–4402.

Nowak, M.A., Lloyd, A.L., Vasquez, G.M., Wiltrout, T.A., Wahl, L.M., Biscofberger, N., Williams, J., Kinter, A., Fauci, A.S., Hirsch, V.M., Lifson, J.D., 1997. Viral dynamics of primary viremia and antiretroviral therapy in simian immunodeficiency virus infection. J. Virol. 71, 7518–7525.

Shapiro, M., Duca, K.A., Lee, K., Delgado-Eckert, E., Hawkins, J., Jarrah, A.S., Laubenbacher, R., Polys, N.F., Hadinoto, V., Thorley-Lawson, D.A., 2008. A virtual look at Epstein-Barr virus infection: simulation mechanism. J. Theor. Biol. 252, 633–648, doi:10.1016/j.jtbi.2008.01.032.

See, H., Wark, P., 2008. Innate immune response to viral infection of the lungs. Paediatr. Respir. Rev. 9, 243–250, doi:10.1016/j.prrv.2008.04.001.

nature genetics

Genome-wide association of *IL28B* with response to pegylated interferon-α and ribavirin therapy for chronic hepatitis C

Yasuhito Tanaka[1,18], Nao Nishida[2,18], Masaya Sugiyama[1], Masayuki Kurosaki[3], Kentaro Matsuura[1], Naoya Sakamoto[4], Mina Nakagawa[4], Masaaki Korenaga[5], Keisuke Hino[5], Shuhei Hige[6], Yoshito Ito[7], Eiji Mita[8], Eiji Tanaka[9], Satoshi Mochida[10], Yoshikazu Murawaki[11], Masao Honda[12], Akito Sakai[12], Yoichi Hiasa[13], Shuhei Nishiguchi[14], Asako Koike[15], Isao Sakaida[16], Masatoshi Imamura[17], Kiyoaki Ito[17], Koji Yano[17], Naohiko Masaki[17], Fuminaka Sugauchi[1], Namiki Izumi[3], Katsushi Tokunaga[2] & Masashi Mizokami[1,17]

The recommended treatment for patients with chronic hepatitis C, pegylated interferon-α (PEG-IFN-α) plus ribavirin (RBV), does not provide sustained virologic response (SVR) in all patients. We report a genome-wide association study (GWAS) to null virological response (NVR) in the treatment of patients with hepatitis C virus (HCV) genotype 1 within a Japanese population. We found two SNPs near the gene *IL28B* on chromosome 19 to be strongly associated with NVR (rs12980275, $P = 1.93 \times 10^{-13}$, and rs8099917, 3.11×10^{-15}). We replicated these associations in an independent cohort (combined *P* values, 2.84×10^{-27} (OR = 17.7; 95% CI = 10.0–31.3) and 2.68×10^{-32} (OR = 27.1; 95% CI = 14.6–50.3), respectively). Compared to NVR, these SNPs were also associated with SVR (rs12980275, $P = 3.99 \times 10^{-24}$, and rs8099917, $P = 1.11 \times 10^{-27}$). In further fine mapping of the region, seven SNPs (rs8105790, rs11881222, rs8103142, rs28416813, rs4803219, rs8099917 and rs7248668) located in the *IL28B* region showed the most significant associations ($P = 5.52 \times 10^{-28}$–2.68×10^{-32}; OR = 22.3–27.1). Real-time quantitative PCR assays in peripheral blood mononuclear cells showed lower *IL28B* expression levels in individuals carrying the minor alleles ($P = 0.015$).

Hepatitis C is a global health problem that affects a significant proportion of the world's population. The World Health Organization estimated that in 1999, there were 170 million HCV carriers worldwide, with 3–4 million new cases appearing each year. HCV infection affects more than 4 million people in the United States, where it represents the leading cause of cirrhosis and hepatocellular carcinoma as well as the leading cause of liver transplantation[1].The American Gastroenterological Association estimated that drugs are the largest direct costs of hepatitis C[1].

The most effective current standard of care in patients with chronic hepatitis C, a combination of PEG-IFN-α with ribavirin, does not produce SVR in all patients treated. Large-scale studies on 48-week-long PEG-IFN-α/RBV treatment in the United States and Europe showed that 42–52% of patients with HCV genotype 1 achieved SVR[2–4], and similar results were found in Japan. However, older patients (greater than 50 years of age) had a significantly lower rate of SVR due to poor adherence resulting from adverse events and laboratory-detectable abnormalities such as neutropenia and thrombocytopenia[5,6]. Specifically, various well-described side effects (such as a flu-like syndrome, hematologic abnormalities and adverse neuropsychiatric events) often necessitate dose reduction, and 10–14% of patients require premature withdrawal from interferon-based therapy[7]. To avoid these side effects in patients who will not be helped by the treatment, as well as to reduce the substantial cost of PEG-IFN-α/RBV treatment, it would be useful to be able to predict an individual's response before or early in treatment. Several viral factors, such as genotype 1, high baseline viral load, viral

[1]Department of Clinical Molecular Informative Medicine, Nagoya City University Graduate School of Medical Sciences, Nagoya, Japan. [2]Department of Human Genetics, Graduate School of Medicine, The University of Tokyo, Tokyo, Japan. [3]Division of Gastroenterology and Hepatology, Musashino Red Cross Hospital, Tokyo, Japan. [4]Department of Gastroenterology and Hepatology, Tokyo Medical and Dental University, Tokyo, Japan. [5]Division of Hepatology and Pancreatology, Kawasaki Medical College, 577 Matsushima, Kurashiki, Japan. [6]Department of Internal Medicine, Hokkaido University Graduate School of Medicine, Sapporo, Japan. [7]Molecular Gastroenterology and Hepatology, Kyoto Prefectural University of Medicine, Kyoto, Japan. [8]National Hospital Organization Osaka National Hospital, Osaka, Japan. [9]Department of Medicine, Shinshu University School of Medicine, Matsumoto, Japan. [10]Division of Gastroenterology and Hepatology, Internal Medicine, Saitama Medical University, Saitama, Japan. [11]Second department of Internal Medicine, Faculty of Medicine, Tottori University, Yonago, Japan. [12]Department of Gastroenterology, Kanazawa University Graduate School of Medicine, Kanazawa, Japan. [13]Department of Gastroenterology and Metabology, Ehime University Graduate School of Medicine, Ehime, Japan. [14]Department of Internal Medicine, Hyogo College of Medicine, Nishinomiya, Japan. [15]Central Research Laboratory, Hitachi Ltd., Kokubunji, Japan. [16]Gastroenterology and Hepatology, Yamaguchi University Graduate School of Medicine, Yamaguchi, Japan. [17]Research Center for Hepatitis and Immunology, International Medical Center of Japan Konodai Hospital, Ichikawa, Japan. [18]These authors contributed equally to this work. Correspondence should be addressed to M.M. (mmizokami@imcjk2.hosp.go.jp).

Received 29 June; accepted 21 August; published online 13 September 2009; doi:10.1038/ng.449